# Case Study on the Dynamic Response of Long Bridges

# Subject to Spatially Varying Ground Motions

by

Jordan Michael Seawright

A Thesis Presented in Partial Fulfillment
of the Requirements for the Degree
Master of Science

Approved July 2019 by the
Graduate Supervisory Committee:

Keith Hjelmstad, Chair
Subramaniam Rajan
Edward Kavazanjian

ARIZONA STATE UNIVERSITY

August 2019

# ABSTRACT

This report analyzed the dynamic response of a long, linear elastic concrete bridge subject to spatially varying ground displacements as well as consistent ground displacements. Specifically, the study investigated the bridge's response to consistent ground displacements at all supports (U-NW), ground displacements with wave passage effects and no soil profile variability (U-WP), and ground displacements with both wave passage effects and soil profile variability (V-WP). Time-history ground displacements were taken from recordings of the Loma Prieta, Duzce, and Chuetsu earthquakes. The two horizontal components of each earthquake time-history displacement record were applied to the bridge supports in the transverse and longitudinal directions. It was found that considering wave passage effects without soil profile variability, as compared with consistent ground displacements, significantly reduced the peak total energy of the system, as well as decreasing the maximum relative longitudinal displacements. The maximum relative transverse displacements were not significantly changed in the same case. It was also found that including both wave passage effects and soil profile variability (V-WP) generally resulted in larger maximum transverse relative displacements, across all earthquake time-histories tested. Similarly, it was found that using consistent ground displacements (U-NW) generally resulted in larger maximum longitudinal relative displacements, as well as larger peak total energy values.

DEDICATION

To Mom and Dad, for never letting me forget who I am.

ACKNOWLEDGMENTS

I would like to thank my advisor, Dr. Keith Hjelmstad, for his invaluable mentorship throughout my degree program. His enthusiasm for engineering mechanics and elegant derivations has shaped my understanding of structural engineering. I would also like to thank Dr. Subramaniam Rajan for sharing his wealth of knowledge in computer-implementation of structural analysis, and for always making the time to answer my questions. I would like to thank Dr. Edward Kavazanjian for his close guidance on the geotechnical aspects of this project, and for helping me to understand the importance and complexity of soils in earthquake engineering. And I would like to thank Dr. Kristen Ward for her generous counsel from day one, and for being there every step of the way.

TABLE OF CONTENTS

Page

CHAPTER Page

LIST OF TABLES

Table Page

TABLE OF FIGURES

Figure Page

Figure Page

Figure Page

Figure Page

# CHAPTER 1: INTRODUCTION AND RESEARCH OBJECTIVES

## 1.1 Spatial Variability

The term spatial variability refers to the phenomenon in which different points in space experience different ground motions from the same seismic event. Variability can arise due the effects of local site geology, which can modify the ground-surface expression of bedrock motions. It can also arise from wave-passage effects, in which a time-shift exists between the ground motions of two different points due to passage of seismic waves through the ground at a finite speed. Spatial variability is always present during seismic events, though most buildings do not have large enough horizontal dimensions to experience any appreciable variation in ground motions. Bridges, however, may have sufficient length to experience a noticeable difference in ground motions.

## 1.2 Case Study Site

The San Mateo-Hayward bridge is the eighth longest bridge in the United States and the longest bridge in California, with a total length of 36,960 ft (7.0 mi, 11.3 km). Additionally, a significant portion of its length is made up by the causeway section that connects to Hayward. The causeway section is very straight, and the water depth beneath it is relatively constant. Furthermore, despite the constant water depth, there is significant variability in the depth of the soil layers beneath the mudline. The bridge sits in close proximity to both the Hayward and San Andreas faults, which run parallel to one another on either side of the bridge. The causeway section of the San Mateo-Hayward bridge is an ideal candidate for a study of spatial variability due to its length of a relatively consistent structural profile, soil site variability, and its proximity to well-studied seismic sources.

## 1.3 Research Objectives

The objective of this research is to observe the changes in dynamic structural response of a long bridge causeway when subjected to spatially varying ground motions. This report studies three different cases—a uniform soil site with no wave passage effects (U-NW), a uniform soil site with wave passage effects (U-WP), and a variable soil site with wave passage effects (V-WP). Three different earthquake time-histories were used to analyze each case, taken from recordings of the Loma Prieta, Duzce, and Chuetsu earthquakes. For each earthquake time-history, the two horizontal components of the displacement record were applied to the transverse and longitudinal directions of the bridge supports. Vertical ground motions were not included in the analyses.

# CHAPTER 2: LITERATURE REVIEW

While the presence of spatial variability ultimately means that different locations in a structure's foundations experience different ground motions, there are several different processes by which variability can arise. Kavazanjian et al. (2011) lists four primary contributors to spatial variability. The first contributor is wave passage effect, wherein the seismic waves, which propagate through the ground at a finite speed, pass different locations in the site at different times, creating a time-shift between the ground motions. The rate at which seismic waves "express themselves" at the surface is referred to as the apparent wave speed, which has a relatively small range of values with a lower bound of 8,250 ft/s (Kavazanjian et al., 2011). When considering wave passage effect for design, a lower bound on the apparent wave speed is generally considered to be conservative, because it produces the greatest time-shift between adjacent supports.

The second contributor to spatial variability is ground motion attenuation. Attenuation relationships describe how ground motions change with respect to the distance from the source. When analyzing a building, an attenuation analysis is usually conducted just once using the site-to-source distance of the structure. However, in a long enough structure, attenuation rates can lead to different ground motion characteristics at different points in the structure. The third contributor to spatial variability is wave-scattering. Wave propagation within the soil can cause differences in both the amplitude and phase of ground motions in a relatively localized area (Kavazanjian et al. 2011).

The fourth contributor to spatial variability is local geologic conditions. As seismic waves propagate from the source up to the ground surface, the waves pass through layers of soil. The ground motions observed at the soil surface can vary greatly

depending on the nonlinear behavior of the soil layers and the thickness of the profile. Yielding of soil layers can cause permanent displacements in the ground surface, which have the potential to induce permanent strains in structures embedded in the ground. Permanent displacements can be particularly problematic in buried pipelines, which are required to displace with the soil.

Kavazanjian et al. concludes that soil profile variability between supports is likely the most important contributor to spatial variability, with the other three cases being negligible in most cases, except for wave passage effect in long structures.

# CHAPTER 3: EXPERIMENTAL METHODS

## 3.1 Experimental Procedure

The following summarizes the general experimental procedure used to investigate the influence of wave passage effects and local site geology on the response of a long bridge causeway, in chronological order. Certain elements of the procedure are elaborated on in subsequent chapters of the report. The structural model was developed as an adaptation of the 2002 addition to the causeway portion of the San Mateo-Hayward Bridge, as described in section 4.1. The geotechnical model was developed using borehole data and geotechnical reports from the area surrounding the bridge site, as described in section 4.3. The initial soil-structure interaction model was developed using LPILE 2015 in conjunction with the geotechnical model and foundation information, as described in section 4.4. The finite element model of the structure was generated in ANSYS Workbench 19.2 using the information from the structural model and the soil-structure interaction model, as described in section 4.2.

An earthquake scenario on the Hayward fault was selected based on a United States Geotechnical Survey (USGS) list of Hayward fault earthquake scenarios (“Hayward Fault Scenarios”, n.d.), and a ground motion attenuation analysis was conducted for the bridge site based on the chosen Hayward fault scenario. A suite of three earthquake time-histories was selected and scaled using the Pacific Earthquake Engineering Research Center (PEER) ground motion database (“PEER Ground Motion”, n.d.), as described in section 5.1. DEEPSOIL 7 was used to conduct a site response analysis, using the outcrop motions from the PEER database as program input, as described in section 5.2. The time-history acceleration data at the ground surface was

collected from the DEEPSOIL output, and the acceleration curves were twice numerically integrated to produce the ground displacement curves at the bridge support locations. The time-history displacements from a single earthquake and test case, namely the Duzce earthquake and the U-NW test case, were applied to the supports of the ANSYS bridge model. The model was analyzed for the Duzce U-NW case, and the maximum relative column-base displacement from the simulation was recorded. The maximum relative column-base displacement was used to determine an updated foundation stiffness, and the process was iterated until convergence of the column-base displacements was achieved.

The ground displacements from each of the nine combinations of a test case (U-NW, U-WP, and V-WP) and an earthquake time-history (Loma Prieta, Duzce, Chuetsu) were applied to the supports of the ANSYS bridge model, and the model was analyzed for each combination. The two horizontal components of each time history were applied to the transverse and longitudinal components of the bridge supports, and the vertical component was not applied. The results of the analysis were post-processed in ANSYS and reported graphically in Chapters 6 and 7 of the report.

## 3.2 Modeling Assumptions

For the scope of this report, the following assumptions are made:

i. *The structure remains elastic*. Nonlinear response of a reinforced concrete structure in the form of yielding or cracking would be expected during a seismic event. However, this report focuses on studying the wave propagation behavior and the effect of spatially varying ground motions on a long, linear-elastic bridge.

ii. *The structure experiences small displacements*. The dynamic analysis is geometrically linear, and small displacements are assumed.

iii. *Seismic waves propagate in the direction of the longitudinal axis of the bridge*. This is generally a conservative assumption, because the difference in the ground motion arrival times between adjacent supports is maximized when the seismic waves propagate parallel to the bridge. It should be noted, however, that this does not guarantee that resonance will not occur at a time shift between zero and the upper limit. Assuming that the waves propagate parallel to the long axis of the bridge is also a reasonable approximation because the San Mateo-Hayward bridge runs nearly perpendicular to the Hayward fault, and the fault is in close proximity to the bridge.

iv. *Structural component rigidities use the gross sectional properties*. The bending and axial rigidities of the structural members are assumed to be equal to the gross moment of inertia and gross area, respectively, multiplied by the modulus of elasticity of 6 ksi concrete. Marsh et al. (2014) states that "Prestressed concrete beams, caps and piles where cracking is not expected" are permitted to be modeled using their gross sectional properties.

v. *No significant ground motion attenuation happens between extents of the bridge*. Spatial variability can arise from ground motion attenuation. However, it is assumed that the bridge site is not large enough to see a significant difference in the bedrock motion due to attenuation.

3.3 Transient Analysis Specifics

Prior to earthquake ground displacements being applied to the base of the structure, self-weight was applied as a ramped load. The vertical gravitational acceleration was ramped up linearly to 1.0 g (32.174 ft/s$^2$) over the first 4.9 sec of the analysis. The ramping was done to minimize the vibrations caused by the application of gravity. During the first 4.9 sec of the analysis, the time step was equal to 0.05 sec. Between 4.9 sec and 5.0 sec, there were no changes in loading. After 4.9 sec, the time step was 0.01 sec. Earthquake time-history displacements were applied beginning at 5.0 sec. Any time-shift in the displacement curves arising from wave-passage effect was applied beginning at 5.0 sec. The loading timeline is illustrated in Figure 3.1.

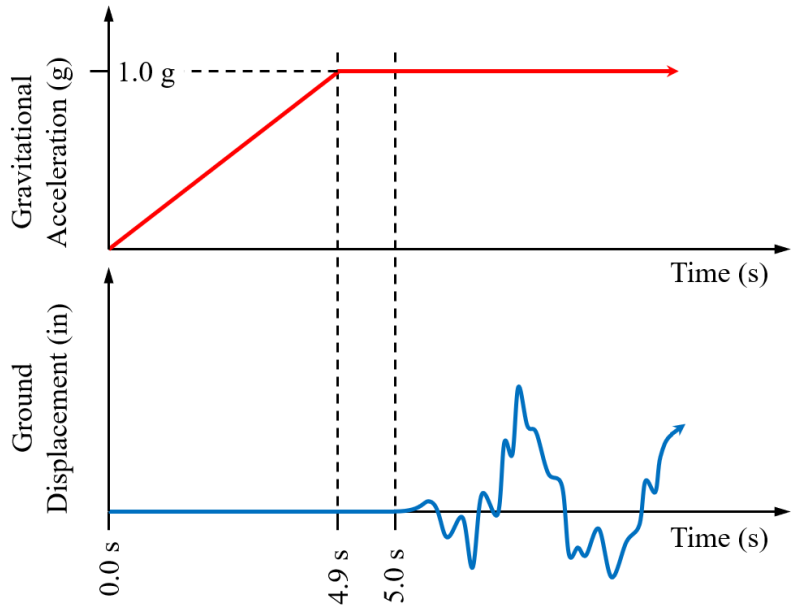


Figure 3.1. Load application timeline.

The transient analysis used the generalized HHT-α method of implicit numerical time-integration, which is an extension of Newmark's method that has improved numerical damping of high-frequency modes. Viscous damping of the structure was

accounted for with Rayleigh damping. Selection of the frequencies for Rayleigh damping is discussed in section 4.5.

# CHAPTER 4: ANALYTICAL MODEL DEVELOPMENT

## 4.1 Structural Model Development

In 2002, CALTRANS completed a widening project on the trestle portion of the San Mateo-Hayward Bridge. The widening was accomplished by erecting a second bridge (hereinafter, "2002 addition") beside the existing bridge to accommodate westbound traffic. The new bridge was constructed entirely from precast, prestressed concrete structural components, except for a concrete slab poured over a precast deck, and partially prestressed bent caps that received a closure pour. The bridge studied in this report was modeled closely after the 2002 addition, with minor modifications.

The substructure of the 2002 addition consisted of 42-inch diameter hollow precast, prestressed concrete piles. Each pile bent contained three piles, spaced at 6.858 m (22.5 ft) on-center. Partially precast U-shaped bent caps connected the tops of the piles, and they served as a ledge for eight 42-inch precast, prestressed concrete bulb-tee girders with an average length of 90 ft. The girders were evenly spaced on the bent caps over a total distance of 16.8 m (55.12 ft). The girders supported precast, prestressed concrete deck panels with a thickness of 80 mm (3.125 in). A 190 mm (7.5 in) slab was poured over the precast deck panels. The tops of the bulb-tee girders contained external steel reinforcement that was encapsulated by the slab during the pour, allowing for the deck and the girders to function as a composite. After the girders were placed on the bent caps, the caps received a closure pour, giving them a final depth of 7 ft. Reinforcement ran continuously from the girders, the piles, and the precast caps into the cast-in-place portion of the caps, forming a fixed connection between the components. The span length of each section was 90 ft, and so pile bents had a spacing of 90 ft on-center. A typical

section of the bridge, taken from a PCI Journal publication discussing the widening project, is shown in Fig. 4.1.

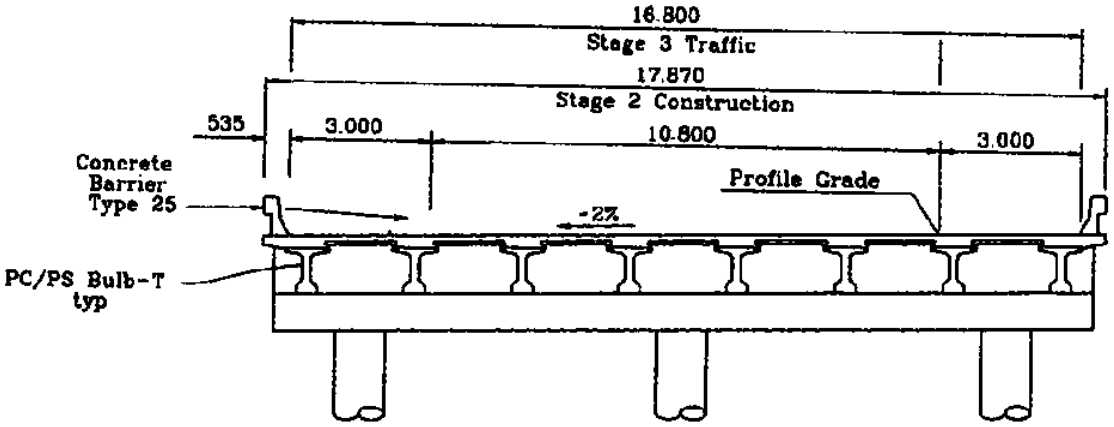


Figure 4.1. Typical section of the bridge added during the San Mateo-Hayward Bridge widening project (PCI Journal).

The model studied in this report was based on the actual 2002 addition, and its structural details were as follows. The substructure consisted of three hollow concrete piles, with a 42 in outer diameter and a 32 in inner diameter, spaced at 22.5 ft on-center. The bent cap was a 7 ft by 7 ft concrete beam, with a length of 56 ft. The piles were assumed to connect rigidly with the bent cap. The prestressed bulb-tee girders were represented by doubly symmetric concrete I-beams (detailed in Fig. 4.2). The flange width and the total depth of the symmetric I-beams were taken to be the same as the upper flange width and the total depth of the 42 in bulb-tees, respectively. The web thickness and flange thickness of the I-beams were solved for by requiring the strong axis moment of inertia and cross-sectional area of the I-beams to be equal to the respective quantities on the bulb-tee girders. The superstructure contained eight I-beams per span, spaced at 8 ft on-center. This spacing placed the centroids of the two end I-beams exactly

at the ends of the bent cap, causing one half of each of the end I-beams to protrude beyond the bent cap. While this would not be acceptable in a physical structure, it provided a suitable approximation of the structure while simplifying the finite element mesh by causing the end-vertices of the bent cap and the end I-beams to coincide. The piles, bent cap, and the I-beams all connected at their respective centroids. The I-beams were assumed to connect rigidly with the bent cap. The bridge deck was represented by a concrete slab with a thickness of 10.6299 in, which was the total thickness of the precast deck and the slab in the 2002 addition. Because the slab was positioned on top of the I-beams, the slab was offset 26.315 in vertically from the centroidal axes of the I-beams. Because centroids of the I-beams were connected to the centroid of the bent cap instead of being situated 9 in above the centroid of the bent cap, as was done with the bulb-tee girders in the 2002 addition, the bent caps protruded several inches above the bridge deck. While this would interfere with the driving surface of the bridge in an actual construction, it was assumed that the lack of offset would not significantly impact the dynamic response. However, the offset of the deck slab from the I-beams was included in the model because the composite action of the I-beams and the slab was expected to significantly impact the bending stiffness of the beam-slab system.

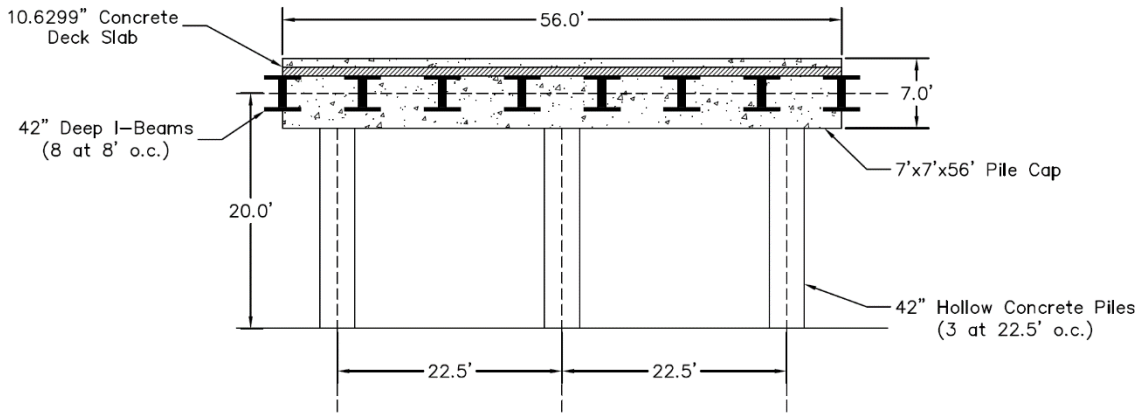


Figure 4.2. Cross-section of bridge model used in the analysis.1

The model included 36 spans, for a total bridge length of 3240 ft (0.988 km). The supports consisted of 35 pile bents and 2 abutments (at the ends). The abutments were modeled the same as the pile bents, except with 4 ft columns. This approximate abutment model was intended to provide a stiffer attachment to the ground at the ends of the bridge, while still accounting for the flexibility of the soil at those points. The abutment at the Hayward end of the bridge was denoted support 0, and the other supports were numbered according to their offset (in spans) from support zero. The coordinate system of the bridge was defined such that the longitudinal axis of the bridge was the positive-x direction, the vertical direction was positive-y, and the transverse direction (out of the page) was positive-z. The support numbering scheme and the coordinate system are illustrated in Figure 4.3.

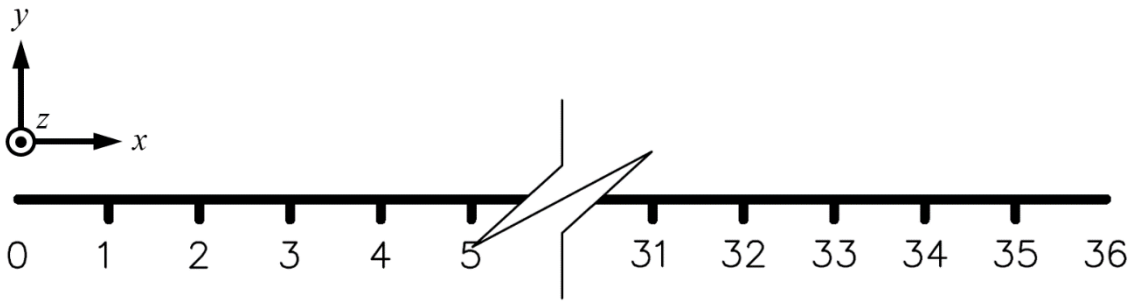


Figure 4.3. Support numbering scheme used in the analysis.

## 4.2 Finite Element Model

The finite element (FE) model of the bridge was created using ANSYS Workbench 19.2. When constructing the geometry of the model, line bodies were used to represent the columns, bent caps, and bridge girders, and surface bodies were used to represent the deck slab. The bridge model geometry was dimensioned as described in section 4.1. The ANSYS geometry of the model is shown in Figure 4.4, looking from underneath the bridge. Additional line bodies were added beneath the columns, parallel to the bent caps, to act as the ground supports, to which time-history displacements were applied.

The columns were assigned a hollow circular cross section with an outer diameter of 42 in and an inner diameter of 32 in. The bent caps were assigned a solid rectangular cross section with side dimensions of 7 ft and 7 ft. The girders were assigned a symmetric I-section with the following dimensions. The top and bottom flange widths were 43 in, the overall depth was 42 in, the top and bottom flange thicknesses were 3.8901 in, and the web thickness was 9.3354 in. The surface body (slab) was given a thickness of 10.6299 in. The cross-sectional properties of the cross-sections are given in Table 4.1. All bodies in the model used 6 ksi concrete as the material (properties described in 4.1).

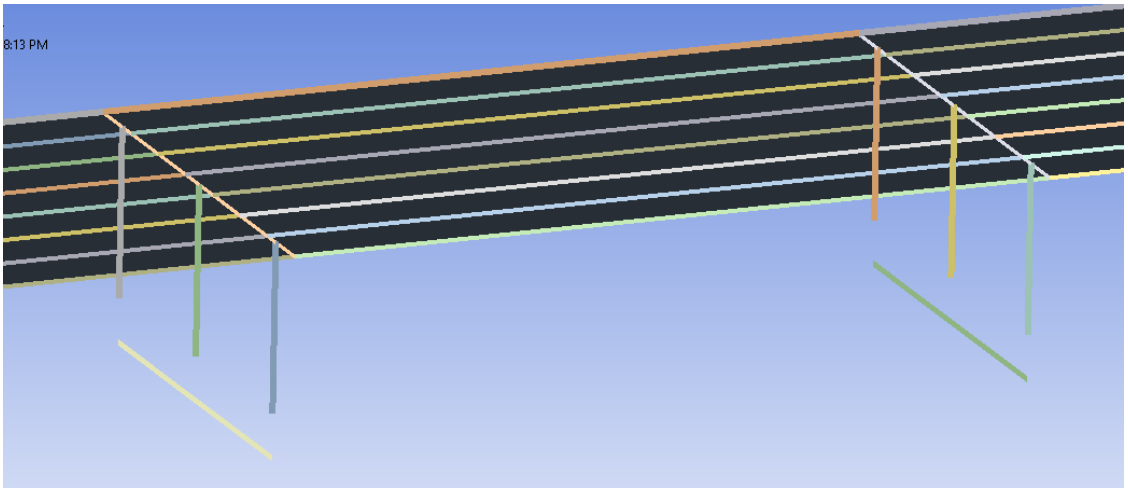


Figure 4.4. ANSYS bridge geometry (view from bottom).

Table 4.1. Cross-sectional properties of line bodies.

| **Location** | **Type** | **Area ($in^2$)** | **$I_{yy}$ ($in^4$)** | **$I_{zz}$ ($in^4$)** |
|---|---|---|---|---|
| Columns | Hollow Circular | 581.17 | 1.0126E+5 | 1.0126E+5 |
| Bent Caps | Rectangular | 7056.0 | 4.1489E+6 | 4.1489E+6 |
| Girders | Sym. I-Section | 654.0 | 1.5307E+5 | 5.3868E+4 |

The line bodies in the model were meshed with beam elements, and the surface body was meshed with shell elements. The ANSYS beam element used in the finite element mesh was BEAM188, which is a 2-noded, cubic, Timoshenko beam element. The ANSYS shell element used in the mesh was SHELL181, which is a 4-noded thin shell element. All elements utilized 6 degrees of freedom per node (UX, UY, UZ, ROTX, ROTY, ROTZ).

A mesh refinement was conducted on the FE model using a static structural analysis. Three FE meshes (Figures 4.5-4.7) were analyzed, and the meshes had the following size characteristics.

1. Mesh 1: 3 elements per column, 5 elements per girder, 3 elements per bent cap, 3 elements in transverse direction for slab, 4.5 elements in the longitudinal direction (every other bent cap was bonded to the midpoint of the shell element, using contact elements).
2. Mesh 2: 5 elements per column, 6 elements per girder, 4 elements per bent cap, 4 elements in transverse direction for slab, 6 elements in the longitudinal direction.
3. Mesh 3: 8 elements per column, 9 elements per girder, 6 elements per bent cap, 6 elements in transverse direction for slab, 9.

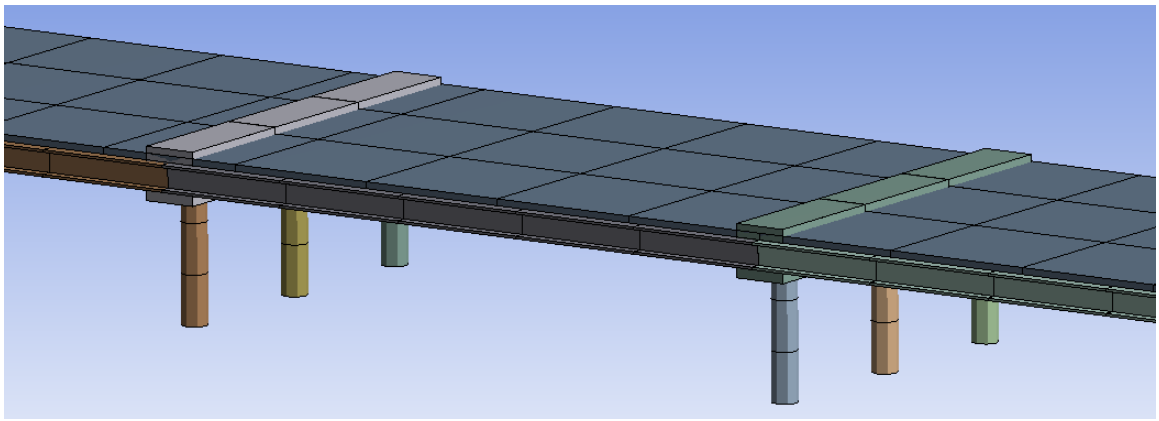

Figure 4.5. Finite Element Mesh 1.

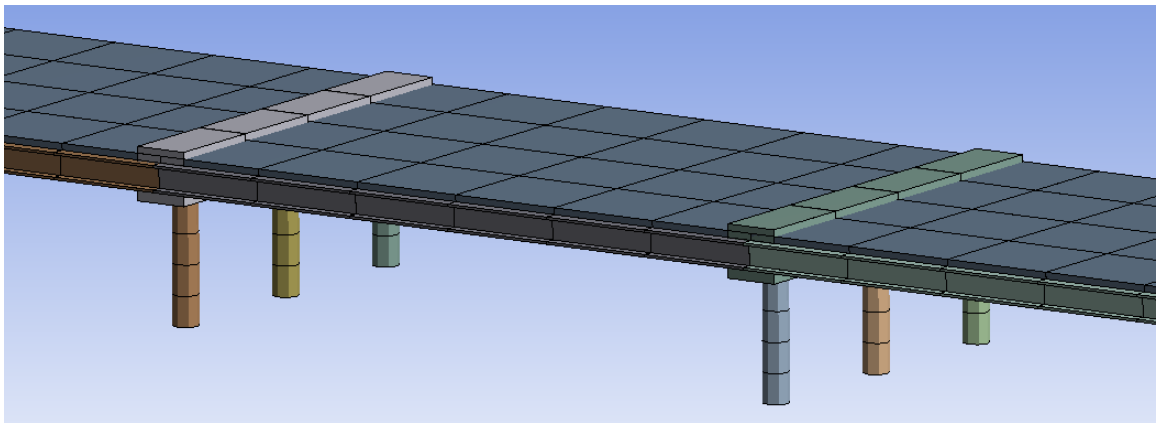

Figure 4.6. Finite Element Mesh 2.

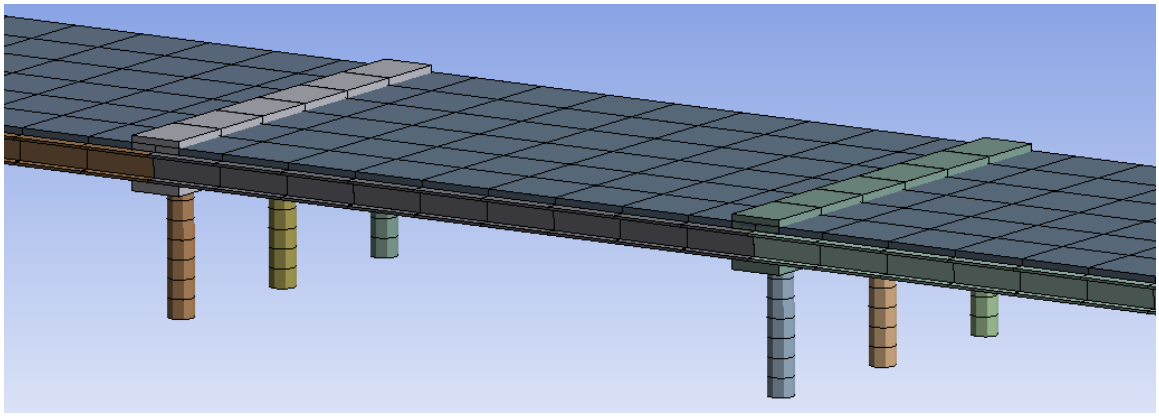

Figure 4.7. Finite Element Mesh 3.

The static load case for the mesh refinement was developed to mimic the relative displacements of the 5th mode shape by applying transverse forces to the pile bents that experienced the largest displacements in the mode shape. The bent caps at supports 4, 18, and 32 each received an applied transverse load of 10,000 lb in the positive-Z direction. The bent caps at supports 11 and 25 each received an applied load of 10,000 lb in the negatve-Z direction. The 5th mode shape is shown in Figure 4.8, and the static loading is shown in Figure 4.9.

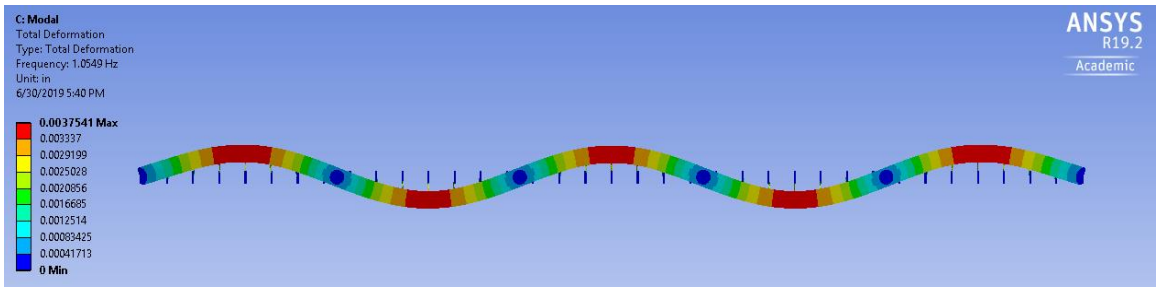


Figure 4.8. The 5th mode shape.

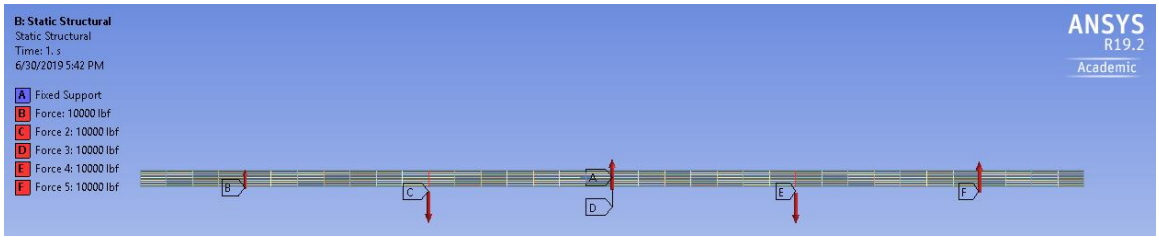


Figure 4.9. Static loading used in the mesh refinement.

All three finite element meshes were analyzed under the static loading described previously. The maximum total displacement of the structure was recorded for each mesh, and the results are summarized in Table 4.2. The deformed shape of mesh 3 is shown in Figure 4.10. The maximum total displacement values from the mesh refinement are plotted with respect to the number of nodes in the model in Figure 4.11.

Table 4.2. Mesh refinement data.

| Mesh # | # of Elements | # of Nodes | Max. Tot. Disp. (in) |
|---|---|---|---|
| 1 | 2432 | 5239 | 0.016262 |
| 2 | 3382 | 6816 | 0.01631 |
| 3 | 5789 | 10660 | 0.0164 |

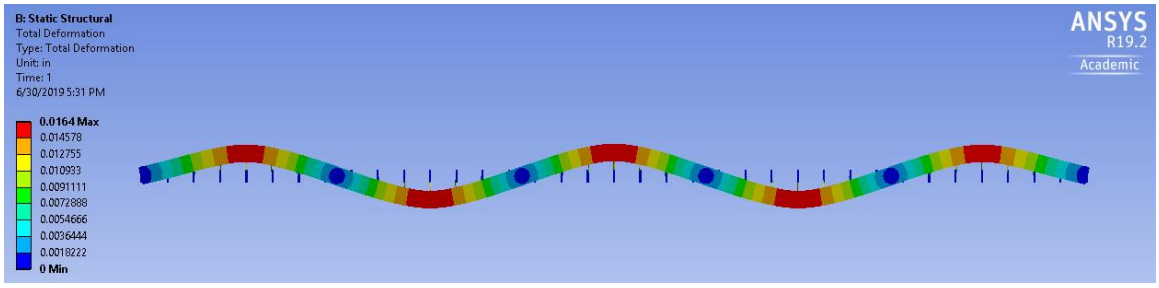


Figure 4.10. Deformed shape for mesh 3.

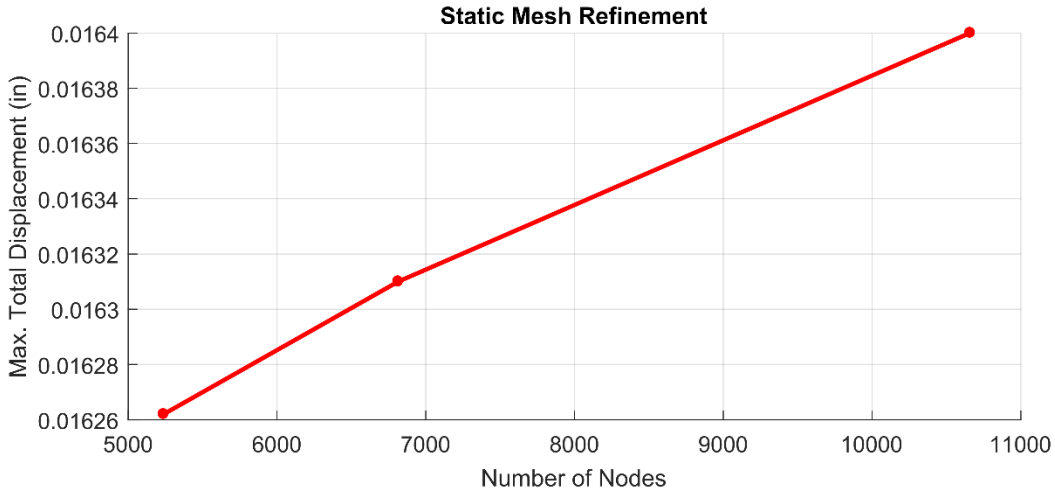


Figure 4.11. Displacement convergence plot.

The convergence plot of the displacement exhibited a slight concave-down curvature, indicating a convergent solution. The model experienced a 0.295% increase in maximum displacement in the refinement from mesh 1 to mesh 2, and it experienced a 0.552% increase in maximum displacement in the refinement from mesh 2 to mesh 3. There was a noticeable increase in the amount of time required to conduct a transient dynamic analysis using mesh 3 when compared with mesh 2. Because mesh 2 had an identical pattern for every span, whereas mesh 1 did not, and there was a significant time advantage of mesh 2 when compared with mesh 3, mesh 2 was selected to be used in the dynamic analyses.

## 4.3 Geotechnical Model Development

Geotechnical information was taken from geotechnical reports and borehole records for locations within the vicinity of the bridge to insure consistency with the San Mateo-Hayward bridge earthquake scenario. The geotechnical report for the widening

project described the predominant layers of the underlying soil to be as follows, in order of increasing depth: Bay mud (soft clay, becoming stiffer with depth), Merrit sand, Posey Formation (mixture of sand and sandy clay), San Antonio Formation (moderately firm clays, sands, and gravel), Alameda Formation (very firm clay to sandy clay to sand and gravel). A simplified soil profile was generated that was consistent with the predominant layers in the geotechnical report. Soil properties were drawn from a geotechnical boring on the shoreline near the Hayward end of the bridge. The parameters of the simplified profile are summarized in Table 4.3.

Table 4.3. Simplified soil profile parameters used in the analysis.

| **Layer** | **Thickness (ft)** | **Soil Type** | **Unit Weight (pcf)** | **PI (%)** | **Cohesion (psf)** | **Friction Angle (°)** |
|---|---|---|---|---|---|---|
| 1 | 20 | Clay | 119.97 | 40 | 800 | ---- |
| 2 | 20 | Clay | 126.88 | 50 | 1200 | ---- |
| 3 | 20 | Sand | 130.9 | ---- | ---- | 42 |
| 4 | 20 | Clay | 128.1 | 20 | 1500 | ---- |
| 5 | 70 | Clay | 130.68 | 35 | 1500 | ---- |

The layer thicknesses given in the table were representative of the layer thicknesses near the shoreline. This soil profile will hereinafter be referred to as profile 0. The test cases involving a uniform soil profile (U-NW and U-WP) assumed that profile 0 was present beneath every support. For the test case with a variable soil profile (V-WP), an idealized variable profile was generated by describing the thickness of each layer as a quadratic function of its linear position along the bridge, with all soil layers beneath the midpoint of the bridge having twice the thickness of the corresponding layers at the ends of the bridge (profile 0). The soil profile is depicted graphically in Fig. 4.12.

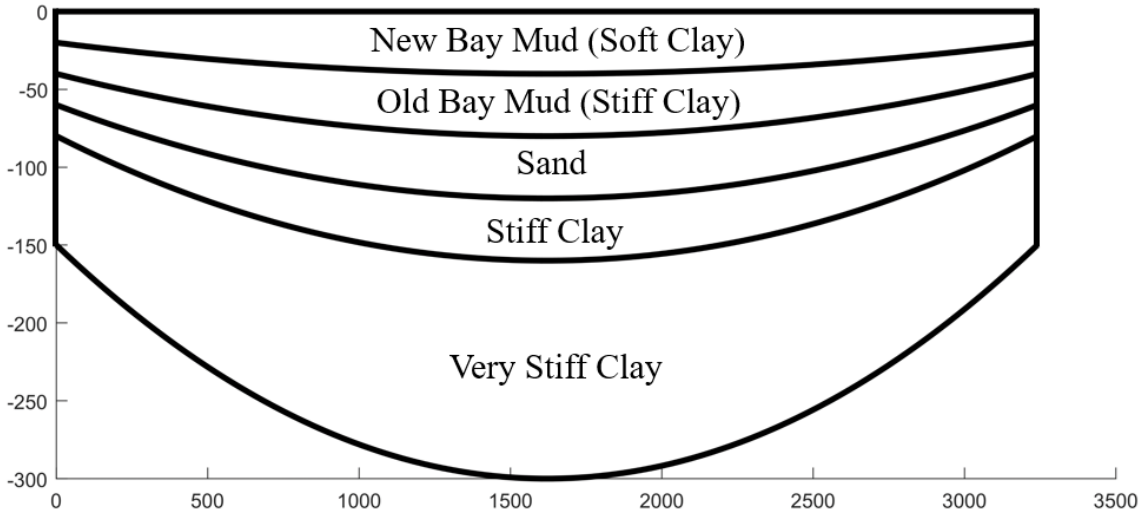


Figure 4.12. Idealized variable soil profile used in analysis.

## 4.4 Soil-Structure Interaction

Depending on the level of rigor used in the analysis, a deep foundation system, such as the driven pile foundation used in the 2002 addition, can be modeled using the entire pile system with nonlinear soil springs applied to the piles at various elevations below the soil surface, or they can be modeled using a simplified, or "substructured" model (Lam and Law, 2000). Lam and Law (2000) lists the accepted techniques for modeling deep foundations, in order of decreasing accuracy, as a) beam supported on nonlinear soil springs, b) coupled foundation stiffness matrix, c) equivalent cantilever model, and d) uncoupled base spring model. Modeling the entire pile length as a beam with nonlinear spring supports requires that each spring receive the input ground motion at the elevation of the spring. Because it provided a balance of modeling effort and accuracy, the coupled foundation stiffness matrix was selected for the analysis (Figure 4.13). The coupled foundation stiffness matrix is a 6x6 matrix that defines the three translational and three rotational stiffnesses, with respect to the relative displacements

and rotations between the ground and the pile at ground level. The matrix contains off-diagonal coupling terms, which distinguish the coupled model from the uncoupled base spring model. The support, which is connected to the column base by the stiffness matrix, then receives the input displacement from the ground level (elevation +0.0). If a foundation contains a pile cap at the ground level, the foundation system can be further substructured to replace all piles in a pile group with a single stiffness matrix. However, since the 2002 addition contains a bent cap with no pile cap at ground level, each column is modeled as having its own coupled foundation stiffness matrix. Because there are 3 piles per support, with a relatively large spacing, kinematic soil-structure interaction and group effects were neglected.

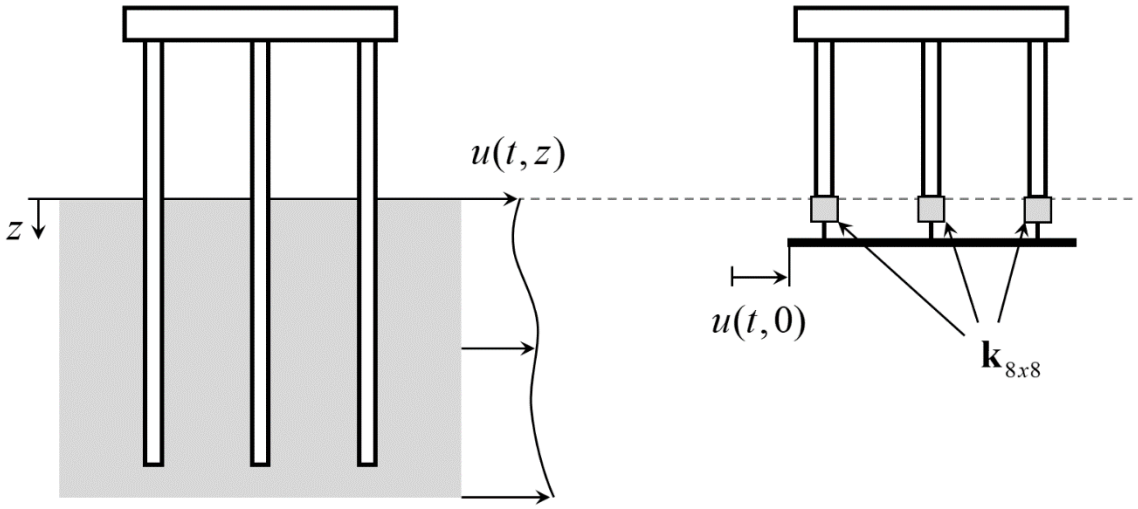


Figure 4.13. Illustration of coupled SSI system.

Because soils exhibit nonlinear behavior, a linear analysis requires that the foundation stiffness matrix be linearized. LPILE 2015 was used to evaluate the load-displacement relationships of the pile embedded in the soil profile developed in section 4.3. A graphic from LPILE depicting the pile embedment in profile-0 is given in Figure

4.13. An initial guess for the foundation stiffness was generated by assuming that a 1000 lb shear force acted at the top of the column at the elevation of the bridge deck (20 ft), generating a moment of 240,000 lb-in. The resulting initial pile-head stiffness matrix ($\mathbf{k}_0$), is given in Equation 1.

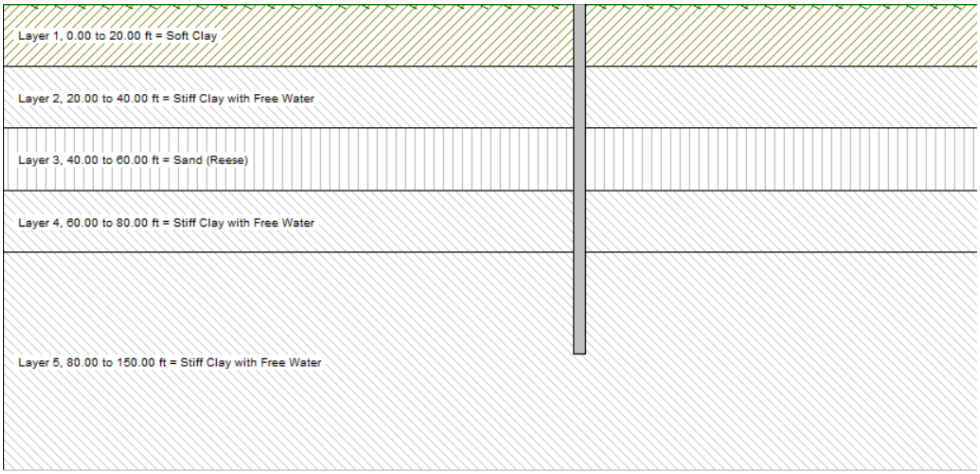


Figure 4.14. LPILE graphic depicting pile embedment.

$$\mathbf{k}_0 = \begin{bmatrix} 7.8956E+05 & & & & & \\ 0 & 1.0000E+12 & & & & \\ 0 & 0 & 7.8956E+05 & & & \\ 0 & 0 & -2.1797E+07 & 5.5482E+09 & & \\ 0 & 0 & 0 & 0 & 1.0000E+12 & \\ -2.1797E+07 & 0 & 0 & 0 & 0 & 5.5482E+09 \end{bmatrix} \quad (1)$$

With the foundation stiffness matrix initialized as defined in Equation 1, the model was analyzed using the Duzce earthquake time-history (see section 5.1) and consistent ground displacements (U-NW). From the analysis results, the maximum relative column-base displacement was recorded. The effective strain factor *n* from Kavazanjian et al. (2011) (Equation 2) was used to reduce the maximum displacement to an effective value, which was then used to calculate the equivalent linear stiffness of the soil-foundation system.

$$n = \frac{(M_w - 1)}{10} \tag{2}$$

Because the Hayward Fault earthquake scenario is a M7.0 (see section 5.1), the effective strain factor is equal to 0.6. Thus, the maximum relative column-base displacement was reduced by 40%, and the reduced displacement was used to re-calculate the pile-head stiffness matrix using LPILE. The resulting stiffness matrix was then implemented in the model, and the model was re-analyzed. This process was repeated iteratively until the maximum relative column-base displacement converged.

Table 4.4. Convergence of pile base displacement.

| **Stiffness Matrix** | **Max. Relative Disp. (in)** | **Max. Rotation (rad)** | **Max. Disp. Pct. Change (%)** |
|---|---|---|---|
| $\mathbf{k}_0$ | 0.71174 | 0.0093804 | ---- |
| $\mathbf{k}_1$ | 1.529 | 0.0065848 | 114.8% |
| $\mathbf{k}_2$ | 1.632 | 0.0071245 | 6.74% |

Because the percent change in maximum relative column-base displacement during the second refinement was 6.74%, down from 114.8% on the first refinement, no further refinements in the stiffness matrix were pursued beyond $\mathbf{k}_2$. The stiffness matrices $\mathbf{k}_1$ and $\mathbf{k}_2$ calculated during the refinement process are given in Equations 3 and 4, respectively.

$$\mathbf{k}_1 = \begin{bmatrix} 2.0680\text{E+}05 & & & & & \\ 0 & 1.0000\text{E+}12 & & & & \\ 0 & 0 & 2.0680\text{E+}05 & & & \\ 0 & 0 & -2.5975\text{E+}07 & 4.5522\text{E+}09 & & \\ 0 & 0 & 0 & 0 & 1.0000\text{E+}12 & \\ -2.5975\text{E+}07 & 0 & 0 & 0 & 0 & 4.5522\text{E+}09 \end{bmatrix} \tag{3}$$

$$\mathbf{k}_2 = \begin{bmatrix} 2.0048E+05 & & & & & \\ 0 & 1.0000E+12 & & & & \\ 0 & 0 & 2.0048E+05 & & & \\ 0 & 0 & -2.5507E+07 & 4.5559E+09 & & \\ 0 & 0 & 0 & 0 & 1.0000E+12 & \\ -2.5507E+07 & 0 & 0 & 0 & 0 & 4.5559E+09 \end{bmatrix} \quad (4)$$

4.5 Modal Analysis and Structural Damping

A modal analysis was conducted on the bridge, and the first 15 natural frequencies were 0.81645 Hz, 0.82676 Hz, 0.85922 Hz, 0.93132 Hz, 1.0579 Hz, 1.2456 Hz, 1.4931 Hz, 1.7951 Hz, 1.927 Hz, 2.1451 Hz, 2.537 Hz, 2.8809 Hz, 2.9653 Hz, 3.3475 Hz, and 3.3642 Hz. Rayleigh damping was used during the dynamic structural analysis, and the following procedure was used to determine the most suitable frequencies to be used in calculating the damping coefficients. To begin, the 5% damped acceleration response spectra was calculated for the transverse component of each earthquake. The period corresponding to the maximum spectral acceleration was taken as the predominant period for the motion. The predominant period for each earthquake was inverted, yielding the predominant frequency of each earthquake. The predominant frequencies in the transverse direction were found to be 5.376 Hz for Loma Prieta, 2.857 Hz for Duzce, and 5.0 Hz for Chuetsu. The mode of response from the bridge at these predominant frequencies was determined by applying a sinusoidal displacement with each predominant frequency uniformly to all supports in the transverse direction. In all three cases, the mode of response to the driving sinusoid closely resembled one of the natural mode shapes of the bridge. The Loma Prieta and Chuetsu predominant frequencies generated very similar modes of response. The Duzce predominant frequency

generated a response mode with fewer points of inflection in the bridge deck. It was determined that the mode shape corresponding to the $13^{th}$ natural frequency of the bridge was the closest to all three response modes, and so a frequency of 2.9653 Hz was selected as the second Rayleigh damping frequency. There appeared to be a distinct "clustering" of natural frequencies in the first four modes, and the third natural frequency of 0.85922 Hz was chosen as the first Rayleigh damping frequency. Using these two natural frequencies, along with a damping ratio of 5%, the mass term was calculated to be 0.418578, and the stiffness term was calculated to be 0.004161.

# CHAPTER 5: GROUND MOTION DEVELOPMENT

## 5.1 Earthquake Scenario

The San Mateo-Hayward Bridge lies in close proximity to the Hayward Fault, which runs parallel to the San Andreas fault on the eastern side of San Francisco Bay. Based on the hazard deaggregation from the National Seismic Hazard Map on the USGS website, a seismic event on the Hayward Fault poses the greatest risk to the trestle portion of the San Mateo-Hayward Bridge, which was taken to be at the coordinates (26.614245, -122.163976). These coordinates lie on the eastern end of the trestle portion of the bridge, slightly offshore. Because the Hayward Fault was determined to be the greatest contributor to the total risk, earthquake scenarios for the Hayward Fault were explored. The USGS website considers three different earthquake magnitudes on the Hayward Fault—a M6.8, a M7.0, and a M7.2 ("Hayward Fault Scenarios", n.d.). The M7.2 scenario involves a rupture of the Hayward and Rodgers Creek faults, and it is significantly less likely than the other two scenarios. The M6.8 and M7.0 scenarios have a similar likelihood of occurrence, because the northern part of the Hayward Fault, which is included in the M7.0 scenarios, has not produced an earthquake in approximately 300 years. The M7.0 scenario with an Oakland epicenter has been referred to as the HayWired earthquake scenario. A map of the fault rupture and resulting ground shaking intensity from the HayWired scenario, taken from the USGS Fact Sheet 2018-3016, is shown in Figure 5.1. Because the M7.0 scenario was larger than, yet had a similar likelihood of occurrence to, the M6.8 event, the M7.0 earthquake scenario was selected for the analysis.

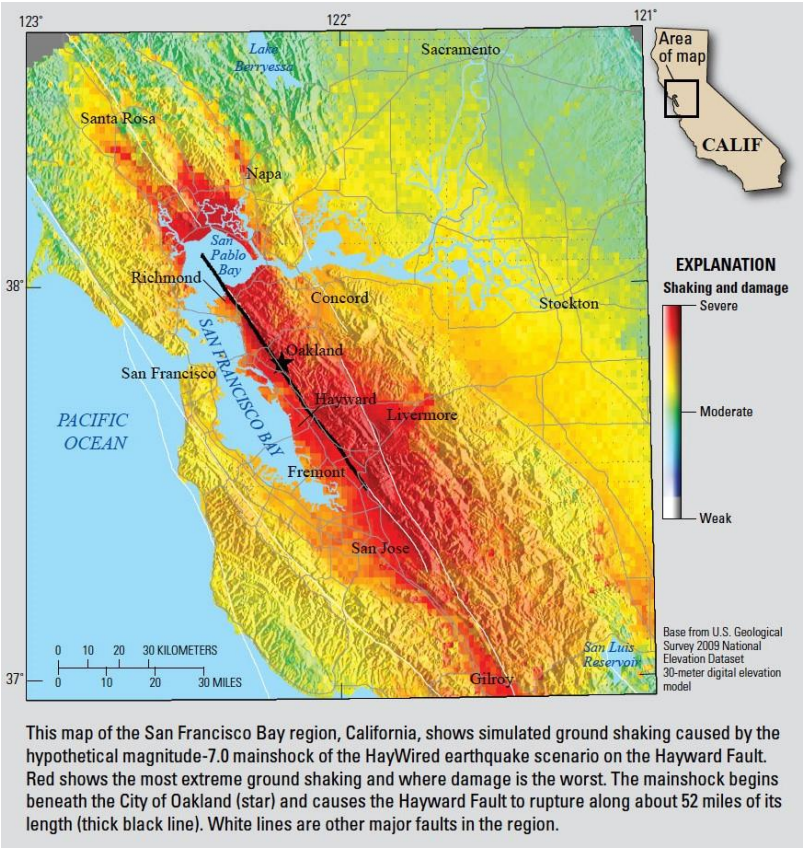


Figure 5.1. Excerpt from the USGS Fact Sheet 2018-3016 entitled "We Can Outsmart the Disaster", depicting the estimated ground shaking from a $M_w$ 7.0 event in the area surrounding the Hayward Fault.

Using Google Maps, the rupture distance from the Hayward Fault to trestle portion of the bridge was estimated to be 10.54 km (6.55 mi). A ground motion attenuation analysis was conducted through the Pacific Earthquake Engineering Research Center (PEER) “NGA-West2” Ground Motion Database, using the Abrahamson-Silva-Kamai (2014) attenuation equations (“PEER Ground Motion”, n.d.), to establish a target spectrum for the design event.

The attenuation tool generated a spectral acceleration response spectrum (target spectrum) based on the Abrahamson-Silva-Kamai (2014) attenuation equations. The PEER database was then used to generate a suite of earthquake time histories that closely

fit the target spectrum. Scaling of the acceleration records was allowed, and the time histories were scaled to minimize the mean squared error (MSE) of the individual records and the average of the records with respect to the target spectrum at three, equally-weighted natural periods of 0.1 s, 1.0 s, and 10.0 s. Five earthquake time-histories were selected from the list, prioritizing MSE, magnitude, and distance to source. Fault-type was taken into consideration, but it was given less weight than the other three metrics. The two horizontal components of each time history were applied to the structural model during the analysis. The selected earthquakes are summarized in Table 5.1.

Table 5.1. Earthquake time-histories selected from the PEER Ground Motion Database.

| **Event** | **Magnitude ($M_w$)** | **Scaling Factor** | **Station** | **Mechanism** | **$R_{rup}$ (km)** | **$V_{s30}$ (m/s)** |
|---|---|---|---|---|---|---|
| Loma Prieta | 6.93 | 0.6522 | San Jose – Santa Teresa Hills | Reverse Oblique | 14.69 | 671.77 |
| Duzce, Turkey | 7.14 | 1.0964 | Lamont 531 | Strike Slip | 8.03 | 638.39 |
| Chi-Chi, Taiwan-03 | 6.2 | 1.6386 | Reverse | Reverse | 9.81 | 671.52 |
| Tottori, Japan | 6.61 | 0.8205 | SMN015 | Strike Slip | 9.12 | 616.55 |
| Chuetsu-oki, Japan | 6.8 | 1.039 | Kawaguchi | Reverse | 27.3 | 640.14 |

Figure 5.2 shows the response spectra of the selected earthquake motions plotted with the target spectrum. The figure shows that, with the recommended scaling factors applied, the time-histories are a very close fit to the target spectrum.

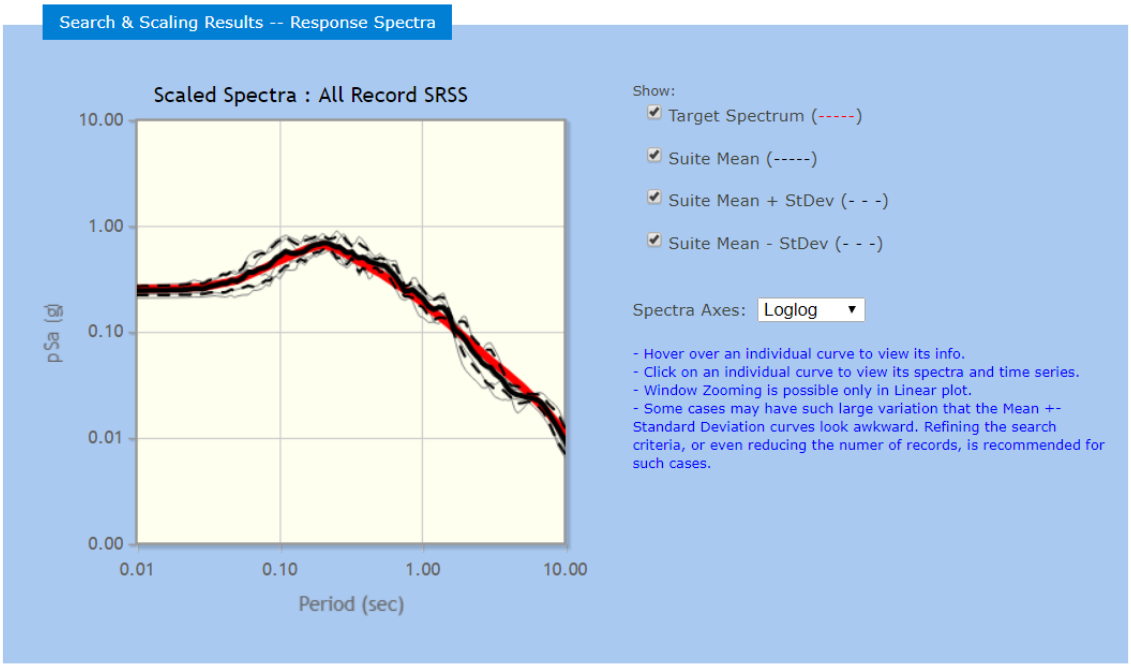


Figure 5.2. Response spectra of the selected earthquake motions plotted with the target spectrum.

After the selections were made, the acceleration time-history data files were downloaded from the PEER database. Of the five earthquake motions downloaded, only the Loma Prieta, Duzce, and Chuetsu time-histories were selected for the analysis. These three motions were selected because they appeared to provide some diversity in the behavior of the displacement curves.

## 5.2 Site Response Analysis

The time-history accelerations selected in section 5.1 were outcrop motions, or motions recorded at sites where bedrock is exposed at the surface. In order to generate the ground motions seen at the top of the soil site developed in section 4.3, a site response analysis was performed using DEEPSOIL 7.0. DEEPSOIL is a program developed at the University of Illinois at Urbana-Champaign that performs linear, equivalent-linear, and nonlinear site response analysis. Given a soil profile and an input bedrock ground motion

time-history, DEEPSOIL outputs acceleration time histories at specified levels within the soil profile. When coupled or decoupled springs are used to represent the SSI system, each spring support should receive an input ground motion corresponding to the elevation of the spring. Therefore, because the coupled spring systems were connected to the piles at the ground level, the acceleration time-history at the ground surface was required.

For the DEEPSOIL analysis, each layer in profile 0 was divided into 10-ft sublayers, forming a total of 15 layers above bedrock. Among these layers were 13 clay layers and 2 sand layers. The soil profile used in the DEEPSOIL analysis is shown in Table 5.3.

Table 5.2. Soil profile information for profile 0, as used for DEEPSOIL input.

| **Layer** | **Thickness (ft)** | **Soil Type** | **Unit Weight (pcf)** | **PI (%)** | **Shear Wave Velocity (ft/s)** |
|---|---|---|---|---|---|
| 1 | 10 | Clay | 119.97 | 40 | 625.65 |
| 2 | 10 | Clay | 119.97 | 40 | 773.85 |
| 3 | 10 | Clay | 126.88 | 50 | 1150.51 |
| 4 | 10 | Clay | 126.88 | 50 | 1227.91 |
| 5 | 10 | Sand | 130.9 | 0 | 1532.89 |
| 6 | 10 | Sand | 130.9 | 0 | 1593.59 |
| 7 | 10 | Clay | 128.1 | 20 | 1458.88 |
| 8 | 10 | Clay | 128.1 | 20 | 1499.84 |
| 9 | 10 | Clay | 130.68 | 35 | 1717.29 |
| 10 | 10 | Clay | 130.68 | 35 | 1754.65 |
| 11 | 10 | Clay | 130.68 | 35 | 1788.96 |
| 12 | 10 | Clay | 130.68 | 35 | 1820.74 |
| 13 | 10 | Clay | 130.68 | 35 | 1850.35 |
| 14 | 10 | Clay | 130.68 | 35 | 1878.11 |
| 15 | 10 | Clay | 130.68 | 35 | 1904.27 |
| Bedrock | 10 | Rock | 150 | N/A | 4986.87 |

The DEEPSOIL analysis was conducted using a nonlinear analysis method, with the option to generate excess porewater pressure disabled. The model was solved in the time-domain using the Newmark-Beta method. The soil model used on all soil layers was the Pressure-Dependent Modified Konder Zelasko (MKZ) model. The hysteretic re/unloading formulation was set to "non-masing re/unloading". The Darendeli (2001) reference curve was used to fit the MKZ parameters for both clays and sands. Clay layers required the input of a plasticity index (PI), whereas the sand layers did not. The fitting procedure was set to "MDRF with UIUC Reduction Factor." Once the nonlinear soil profile model was generated, it was analyzed for all six earthquake time-history acceleration files (three earthquakes, with two directions each). For each profile, the resulting ground-level acceleration time-history was generated and then twice numerically integrated to create the displacement curves. The resulting ground-level displacement curves are shown in Figures 5.3, 5.4, and 5.5 below. Each figure contains all locations in the quadratic profile plotted together, and permanent displacements are visible throughout.

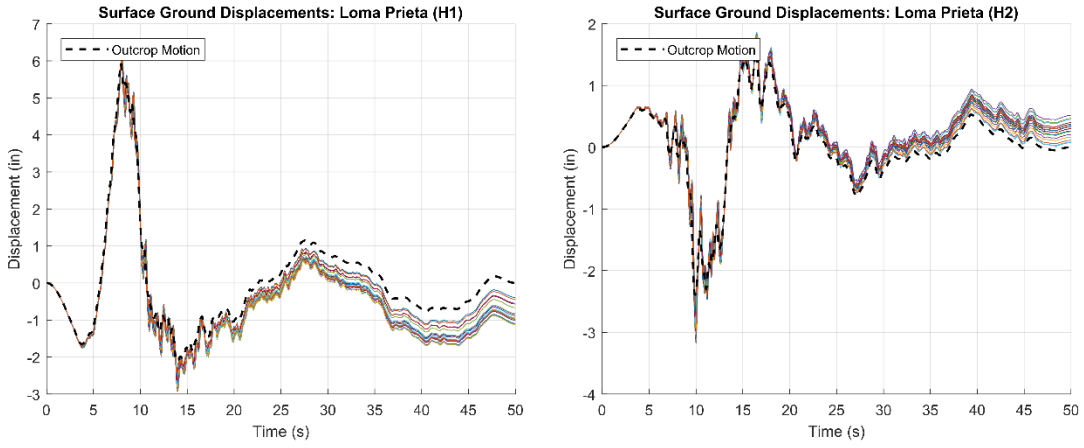


Figure 5.3. Ground-level displacement time-history for Loma Prieta.

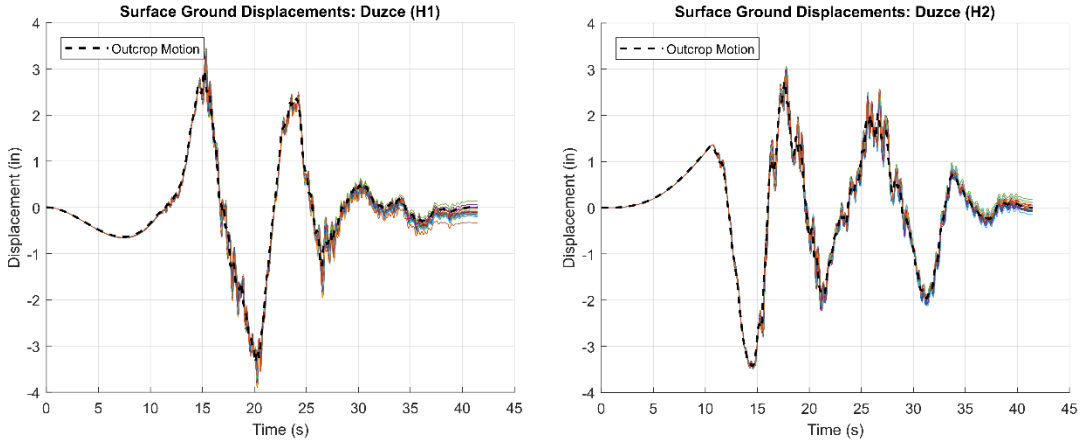


Figure 5.4. Ground-level displacement time-history for Duzce.

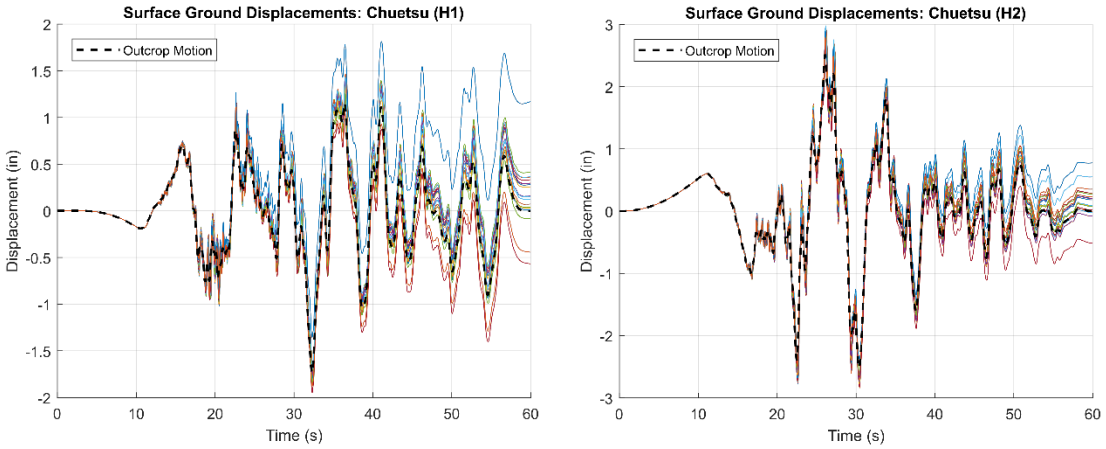


Figure 5.5. Ground-level displacement time-history for Chuetsu.

# CHAPTER 6: RESULTS OF DYNAMIC ANALYSES

## 6.1 Model Subject to Consistent Ground Displacements

This section summarizes the results collected from the simulations with consistent ground displacements (U-NW). For each of the earthquake time-histories, the maximum absolute value of the transverse relative bent cap displacement was recorded at each support location and plotted in Figure 6.1. Chuetsu (blue) produced the largest displacement at nearly every support, with a maximum displacement of 3.629 in at support 12. Duzce (red) produced a maximum displacement 2.708 in at support 8. Loma Prieta (green) produced the smallest displacement at nearly every support, with a maximum displacement of of 2.101 in at support 25. The maximum displacement values were nearly symmetric about the midpoint of the bridge. In all three cases, the maximum displacement occurred at a support at least six spans away from the center support.

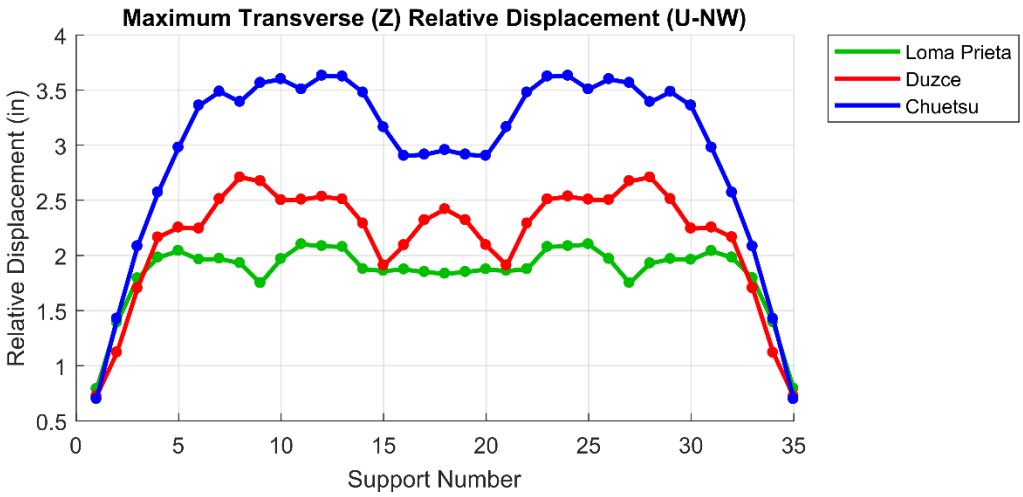


Figure 6.1. Maximum absolute transverse relative bent cap displacement.

The maximum absolute value of the longitudinal relative bent-cap displacement was recorded for each support and plotted in Figure 6.2. Loma Prieta produced a maximum displacement of 3.063 in at support 17. Duzce produced a maximum displacement of 2.524 in at support 19. Chuetsu produced a maximum displacement of 2.123 in at support 19. For all three earthquakes, the maximum displacement occurred at a support near the midpoint of the bridge, and the displacements decreased toward the ends of the bridge.

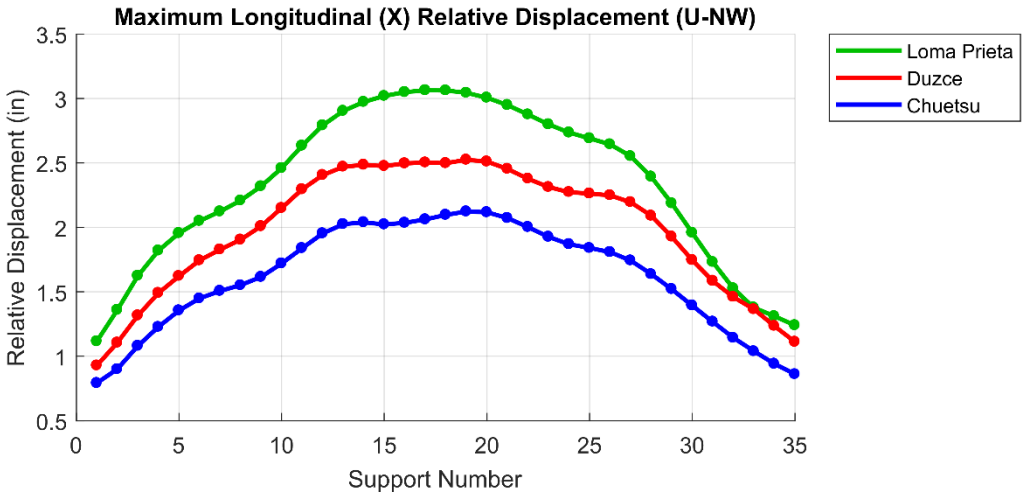


Figure 6.2. Maximum absolute longitudinal relative bent cap displacement.

The maximum total bending moment was recorded for the columns at each support at plotted in Figure 6.3. Loma Prieta produced a maximum moment of 4.671E+7 lb-in at support 19. Duzce produced a maximum moment of 3.838E+7 lb-in at support 19. Chuetsu produced a maximum moment of 3.476E+7 lb-in at support 12. The maximum moment curves generated from the Loma Prieta and Duzce earthquakes appeared to have maximum values near the midpoint of the bridge and decreasing values toward the supports.

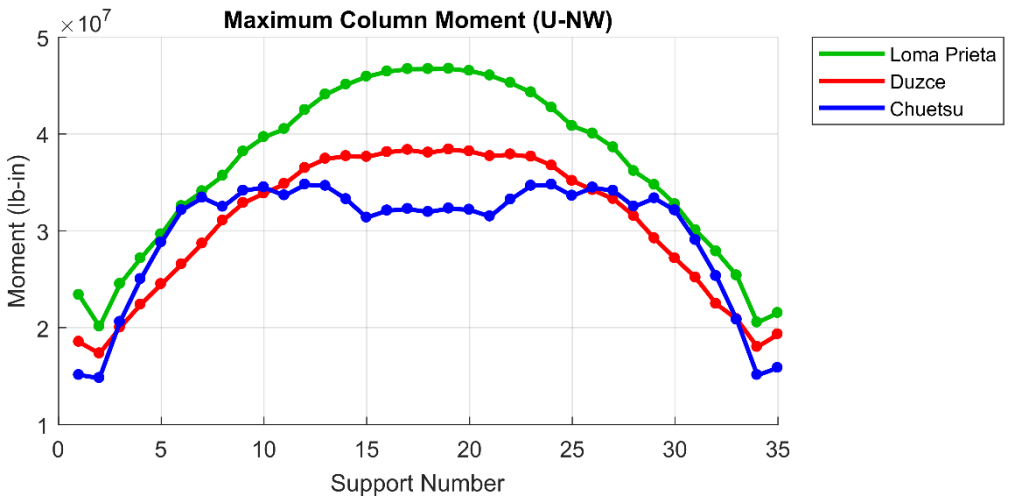


Figure 6.3. Maximum total column bending moment.

The time-history graphs of the relative transverse displacements of the bent caps are given in Figures 6.4, 6.5, and 6.6, which give the displacement response for Loma Prieta, Duzce, and Chuetsu, respectively. Each graph contains the time-history displacements of all supports plotted in the same window. The curves are color-coded such that the curve representing the response of support 1 is black, the curve representing the response of support 35 is red, and the color of the curve representing each support in between is a linear interpolation between supports 1 and 35. Note: Hereinafter, this color-coding scheme will be referred to as "Graph Format A". The response in all three cases appears to be periodic, and the supports appear to vibrate with proportional displacements. Note that, due to the curves being plotted in order of ascending support numbers, the black and dark red curves are mostly obscured by the light red curves in this case.

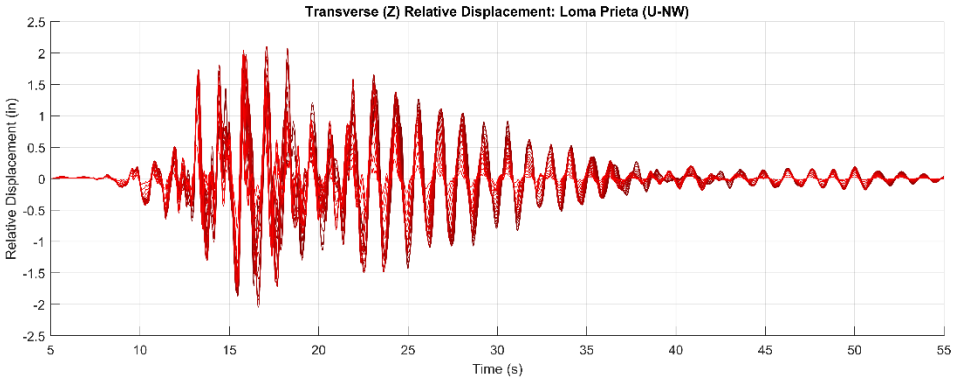


Figure 6.4. Relative transverse bent cap displacements for Loma Prieta.

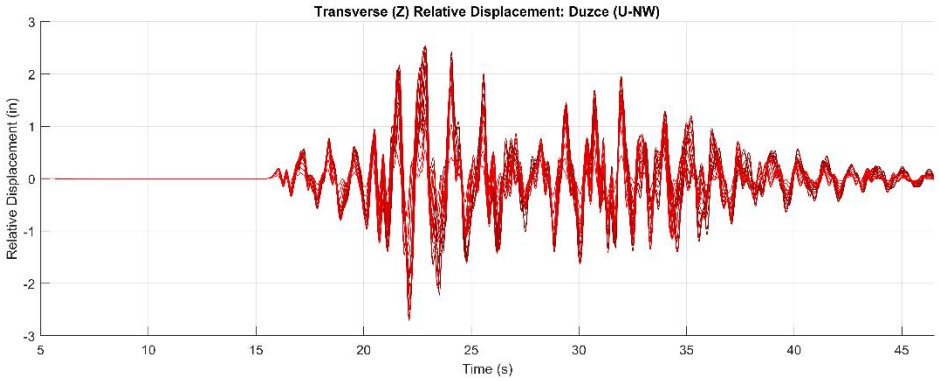


Figure 6.5. Relative transverse bent cap displacements for Duzce.

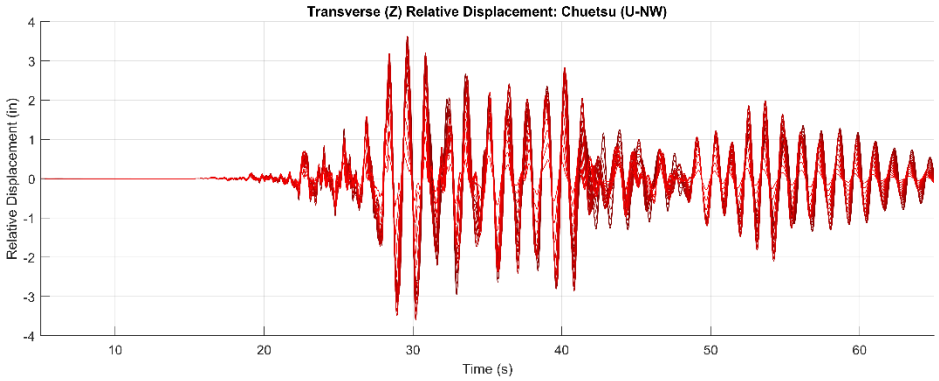


Figure 6.6. Relative transverse bent cap displacements for Chuetsu.

The time-history graphs of the relative longitudinal displacements of the bent caps are given in Figures 6.7, 6.8, and 6.9. The graphs are color-coded using Graph Format A. As with the transverse displacement curves, the supports appear to vibrate with proportional displacements and no noticeable phase shift. The longitudinal vibrations appear to have higher frequencies than the corresponding transverse vibrations.

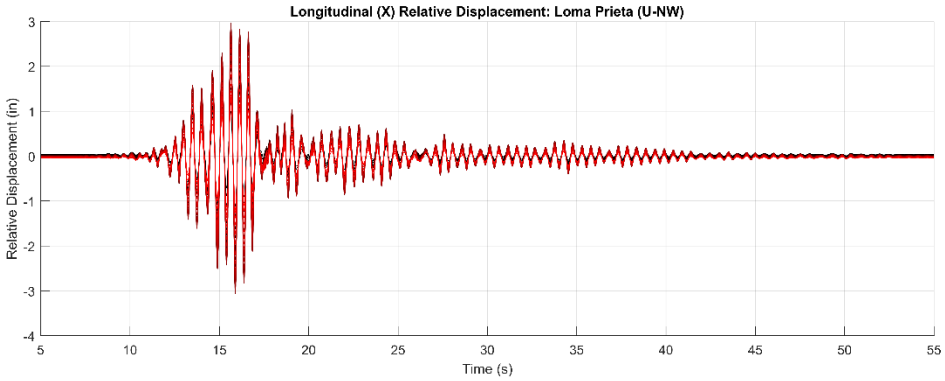


Figure 6.7. Relative longitudinal transverse bent cap displacements for Loma Prieta.

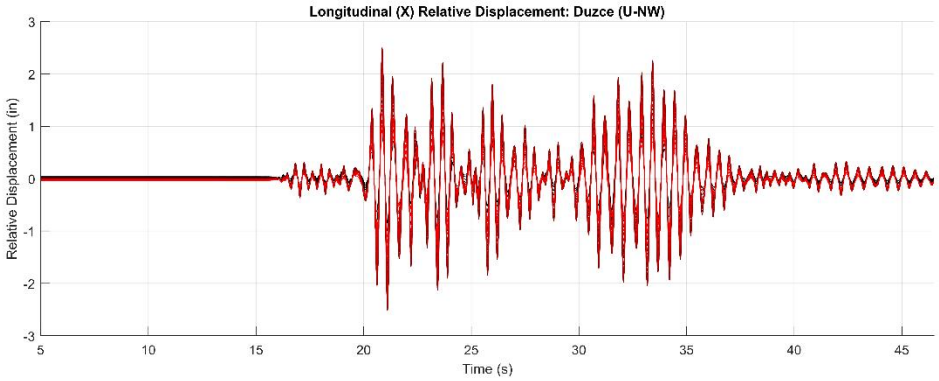


Figure 6.8. Relative longitudinal transverse bent cap displacements for Duzce.

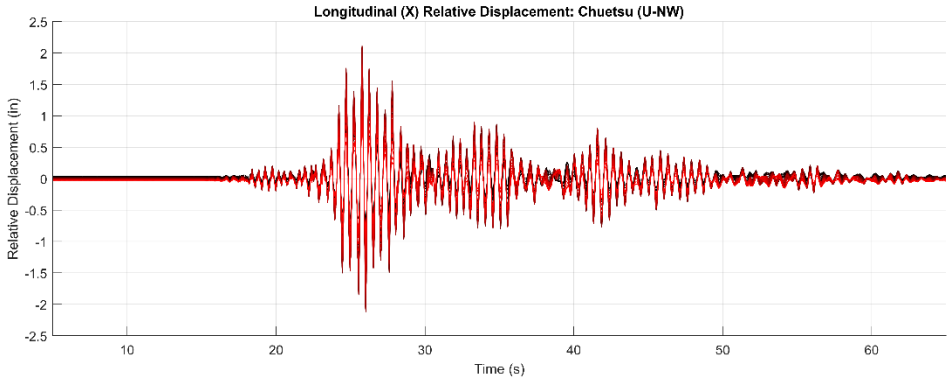


Figure 6.9. Relative longitudinal bent cap displacements for Chuetsu.

The kinetic, strain, and total energy curves are shown in Figures 6.10, 6.11, and 6.12 for Loma Prieta, Duzce, and Chuetsu, respectively. Loma Prieta produced a maximum total energy of 8045.38 BTU at 15.75 sec. Duzce produced a maximum total energy of 5689.16 BTU at 20.98 sec. Chuetsu produced a maximum total energy of 3419.95 BTU at 25.64 sec. Note that, since vertical ground motions were not applied and the analysis was geometrically linear, gravitational potential energy was assumed to be negligible.

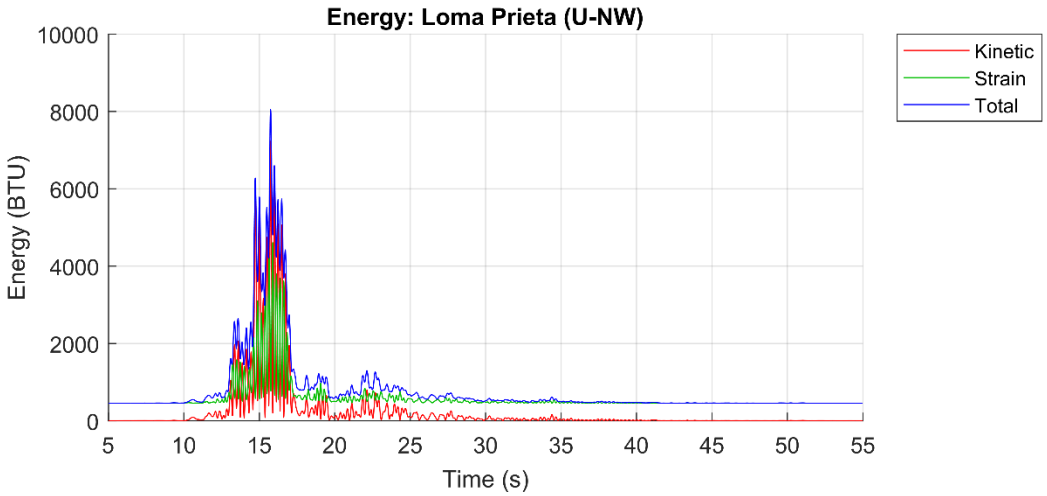


Figure 6.10. Kinetic, strain, and total energy for Loma Prieta.

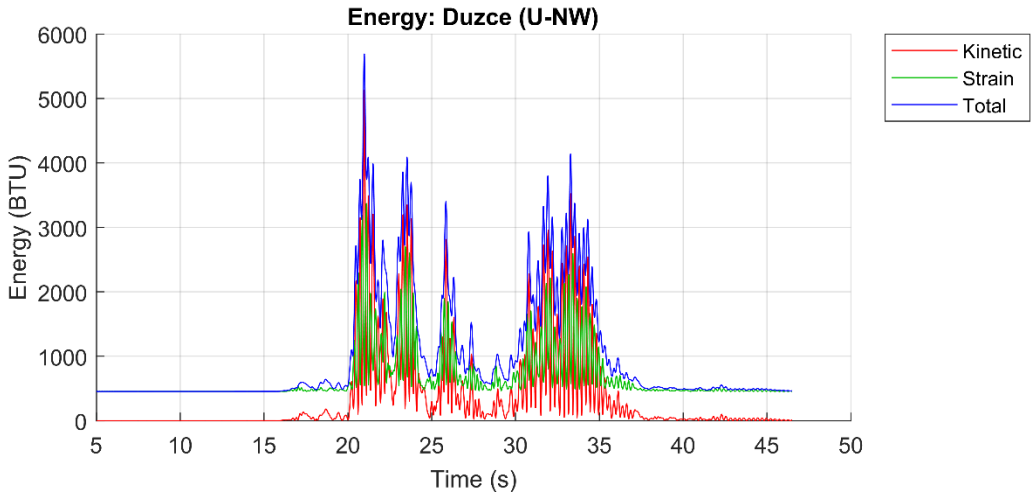


Figure 6.11. Kinetic, strain, and total energy for Duzce.

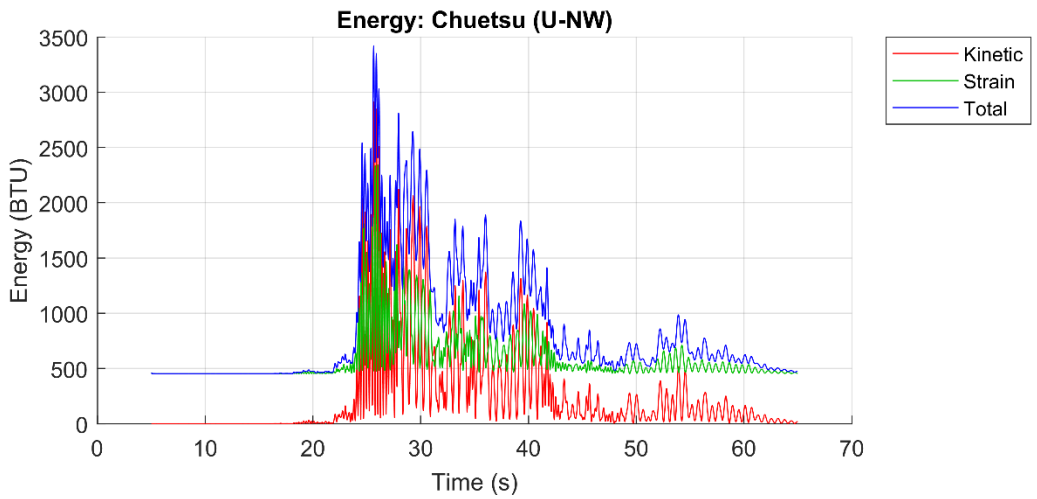


Figure 6.12. Kinetic, strain, and total energy for Chuetsu.

## 6.2 Model Subject to Wave-Passage Effect on a Uniform Soil Profile

This section summarizes the results collected from the simulations with wave passage effect and a uniform soil site (U-WP). The maximum absolute value of the transverse relative bent-cap displacement for each support is shown in Figure 6.13. Chuetsu (blue) produced the largest displacement at every support, with a maximum displacement of 3.989 in at support 26. Duzce (red) produced a maximum displacement 2.768 in at support 12. Loma Prieta (green) produced the smallest displacement at nearly every support, with a maximum displacement of 2.251 in at support 8. The maximum displacement curves appeared to decrease toward the ends of the bridge, though the curves lacked the symmetry observed in the U-NW case.

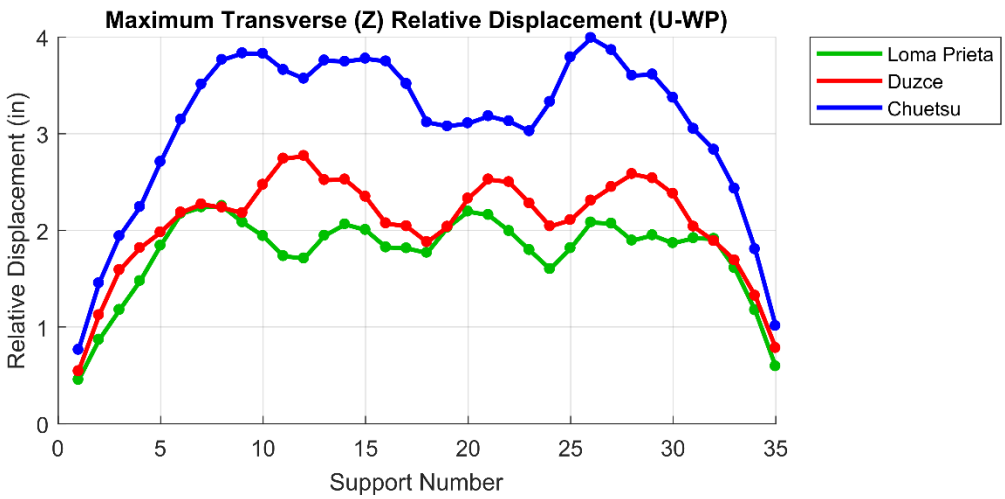


Figure 6.13. Maximum absolute transverse relative bent cap displacement.

The maximum absolute value of the longitudinal relative bent-cap displacement was recorded for each support and plotted in Figure 6.14. Loma Prieta produced a maximum displacement of 0.3418 in at support 35. Duzce produced a maximum displacement of 0.4116 in at support 7. Chuetsu produced a maximum displacement of 0.3262 in at support 7. For all three earthquakes, the maximum displacement occurred at a support near the ends of the bridge, and the displacements decreased toward the midpoint of the bridge.

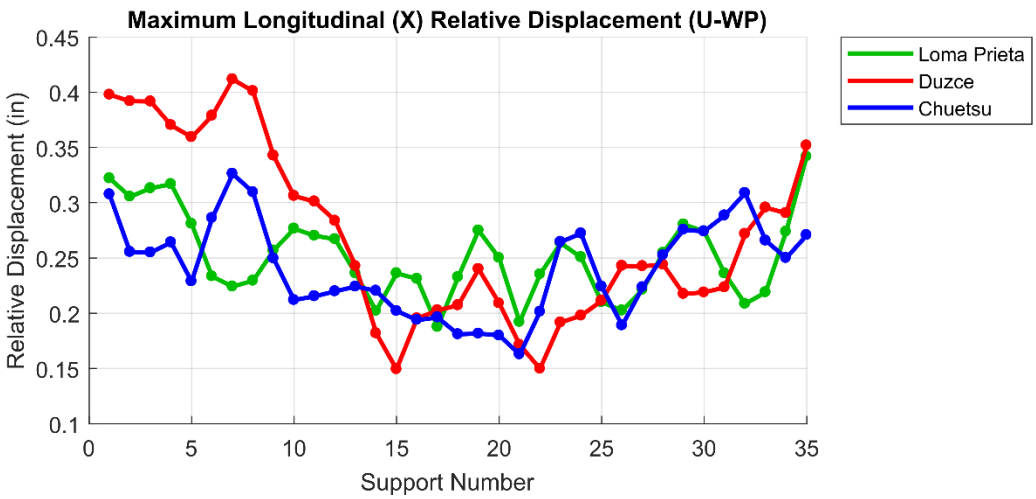


Figure 6.14. Maximum longitudinal relative bent cap displacement

The maximum total bending moment was recorded for the columns at each support at plotted in Figure 6.15. Loma Prieta produced a maximum moment of 2.161E+7 lb-in at support 8. Duzce produced a maximum moment of 2.647E+7 lb-in at support 12. Chuetsu produced a maximum moment of 3.809E+7 lb-in at support 26. The maximum column moment values appeared to decrease toward the ends of the bridge. The shapes of all three maximum moment curves appear to resemble the shapes of the corresponding maximum transverse relative displacement curves.

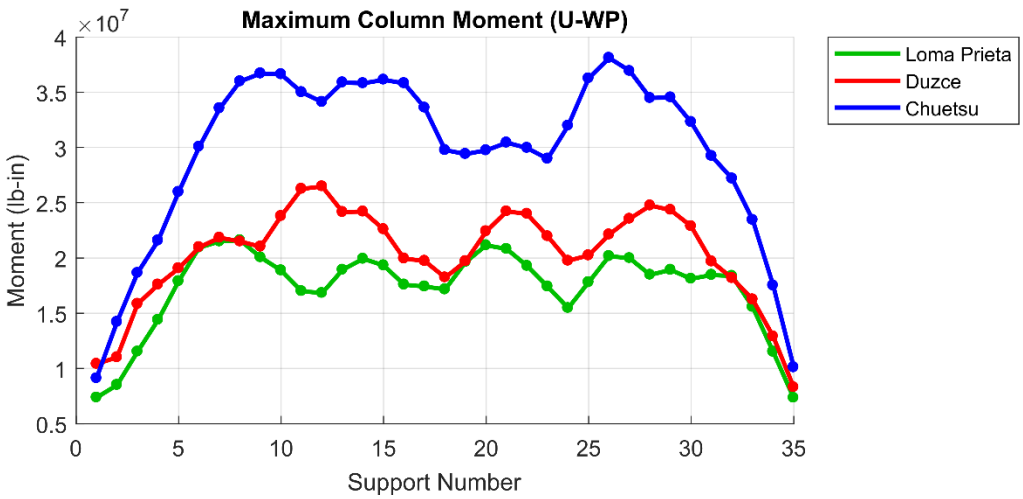


Figure 6.15. Maximum total column bending moment.

The time-history graphs of the relative transverse displacements of the bent caps are given in Figures 6.16, 6.17, and 6.18, which give the displacement response for Loma Prieta, Duzce, and Chuetsu, respectively. Each graph contains the time-history displacements of all supports plotted in the same window. The curves are color-coded according to *Graph Format A*. The response in all three cases appears to be periodic, and the supports appear to vibrate with proportional displacements. In this case, there appears to be a delay (phase shift) between the lower support numbers (dark shades) and the higher support numbers (light shades).

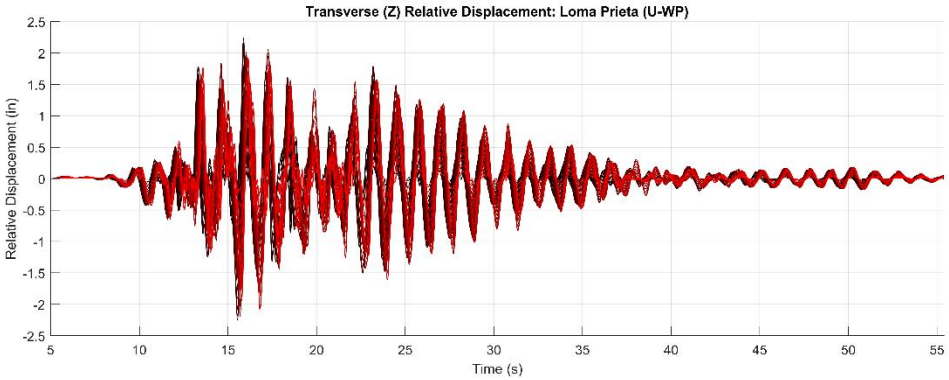


Figure 6.16. Relative transverse bent cap displacements for Loma Prieta.

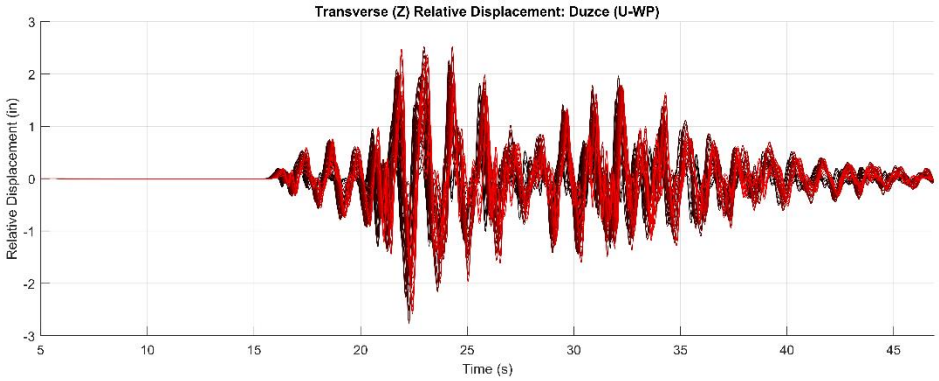


Figure 6.17. Relative transverse bent cap displacements for Duzce.

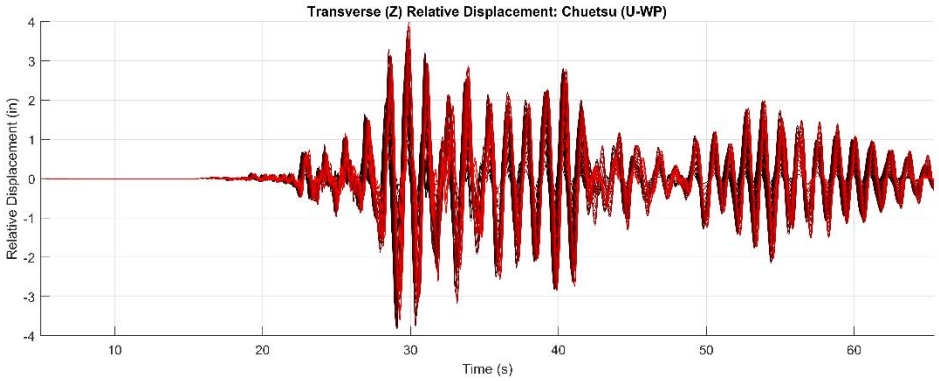


Figure 6.18. Relative transverse bent cap displacements for Chuetsu.

The time-history graphs of the relative longitudinal displacements of the bent caps are given in Figures 6.19, 6.20, and 6.21, which give the displacement response for Loma Prieta, Duzce, and Chuetsu, respectively. The graphs are color-coded using *Graph Format A*. The longitudinal vibrations appear to have higher frequencies than the corresponding transverse vibrations. In contrast to the transverse vibrations, the longitudinal vibrations appear to be highly chaotic, with little correlation between motions at different points along the bridge.

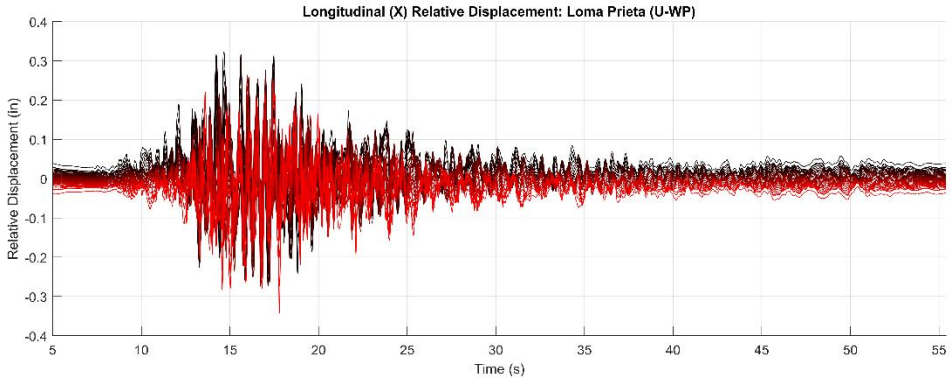


Figure 6.19. Relative longitudinal bent cap displacements for Loma Prieta.

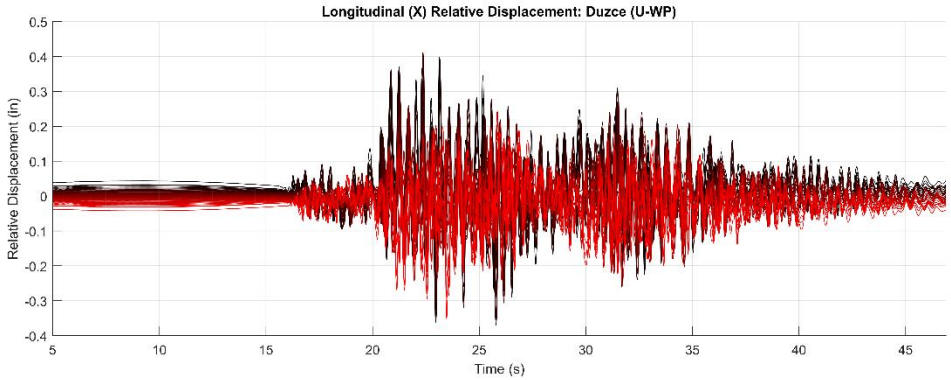


Figure 6.20. Relative longitudinal bent cap displacements for Duzce.

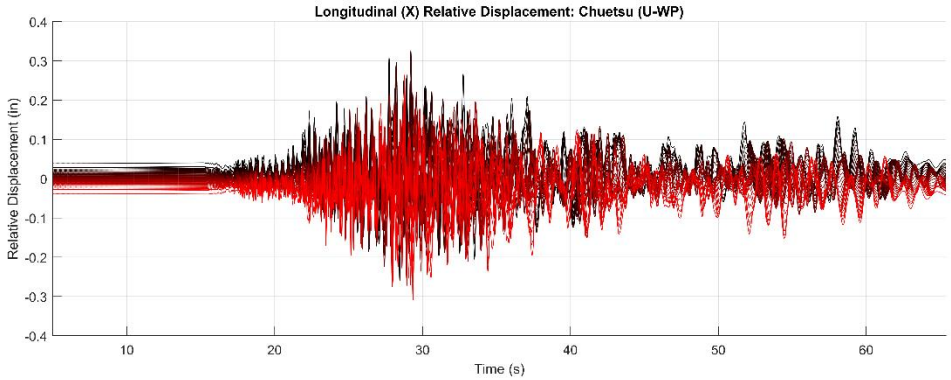


Figure 6.21. Relative longitudinal bent cap displacements for Chuetsu.

The kinetic, strain, and total energy curves are shown in Figures 6.22, 6.23, and 6.24 for Loma Prieta, Duzce, and Chuetsu, respectively. Loma Prieta produced a maximum total energy of 1400.31 BTU at 14.94 sec. Duzce produced a maximum total energy of 1699.28 BTU at 23.29 sec. Chuetsu produced a maximum total energy of 2345.37 BTU at 29.47 sec.

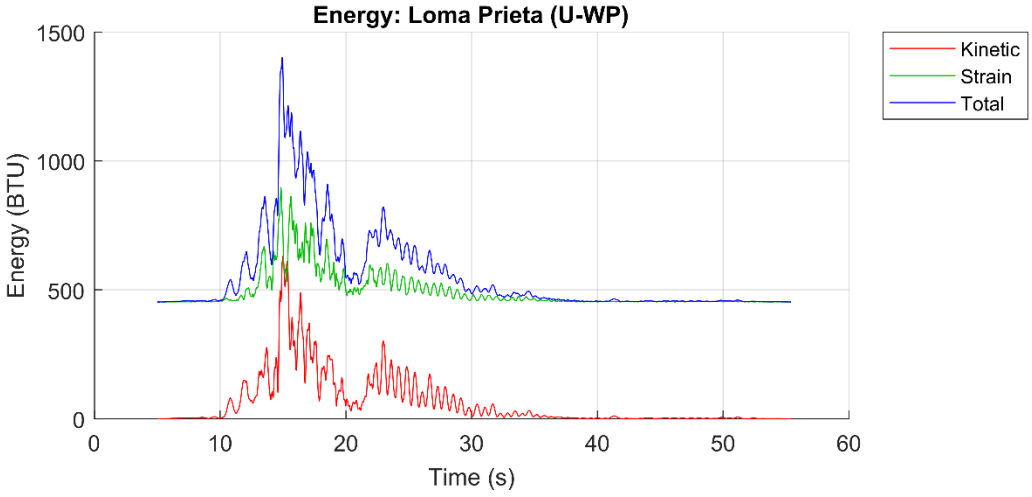


Figure 6.22. Kinetic, strain, and total energy for Loma Prieta.

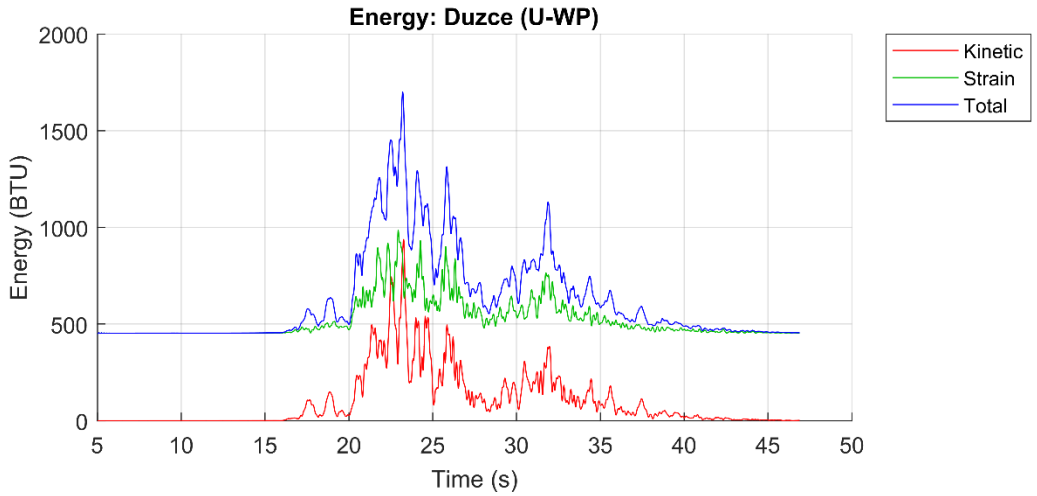


Figure 6.23. Kinetic, strain, and total energy for Prieta.

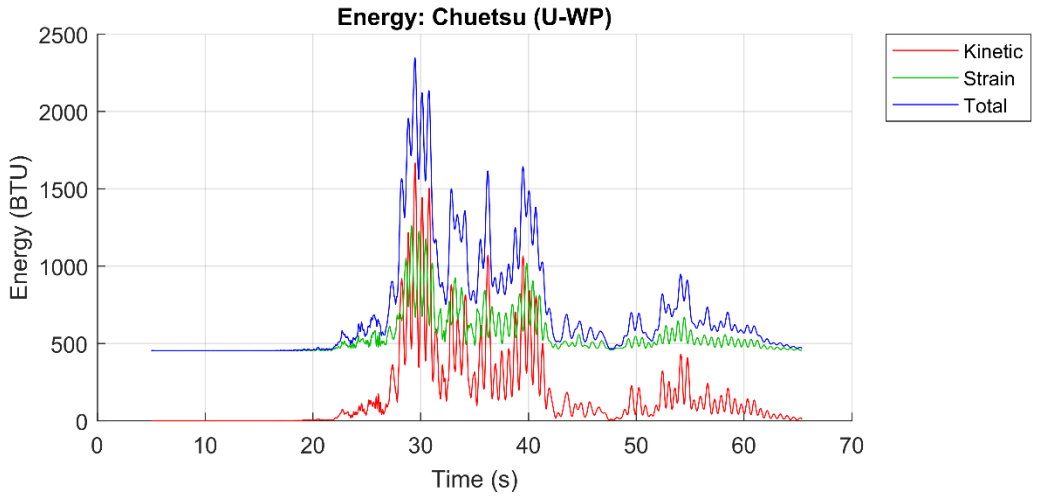


Figure 6.24. Kinetic, strain, and total energy for Chuetsu.

## 6.3 Model Subject to Wave-Passage Effect on a Variable Soil Profile

This section summarizes the results collected from the simulations with wave passage effect and a variable soil site (V-WP). The maximum absolute value of the transverse relative bent-cap displacement for each support is shown in Figure 6.25. Chuetsu (blue) produced the largest displacement at every support, with a maximum displacement of 5.046 in at support 10. Duzce (red) produced a maximum displacement

3.723 in at support 12. Loma Prieta (green) produced generally similar maximum displacements to Duzce, with a maximum displacement of 3.242 in at support 10. The maximum displacement curves appeared to decrease toward the ends of the bridge.

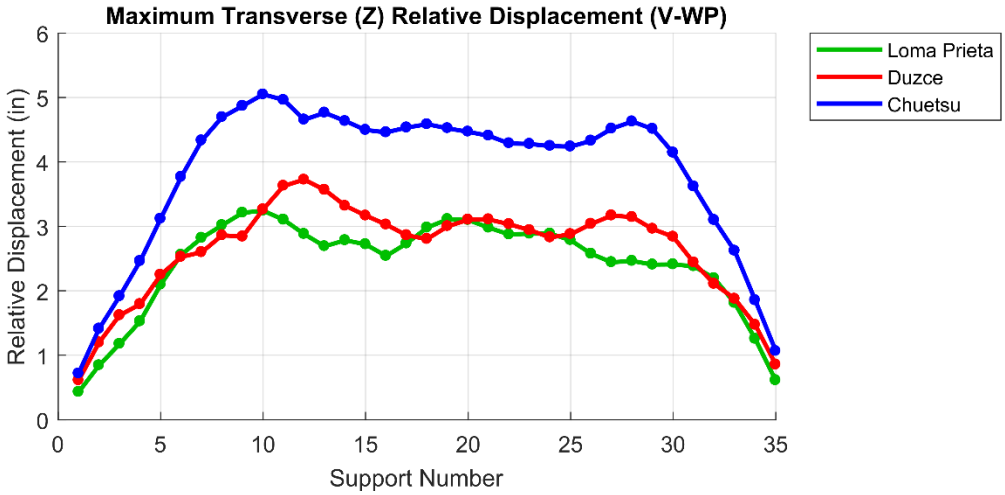


Figure 6.25. Maximum absolute transverse relative bent cap displacement.

The maximum absolute value of the longitudinal relative bent-cap displacement was recorded for each support and plotted in Figure 6.26. Loma Prieta produced a maximum displacement of 1.742 in at support 18. Duzce produced a maximum displacement of 1.523 in at support 10. Chuetsu produced a maximum displacement of 1.474 in at support 35. For all three earthquakes, the maximum displacement generally increased toward the midpoint of the bridge. The Chuetsu earthquake, however, produced abnormally high longitudinal displacements at supports 1 and 35 (the supports nearest the abutments).

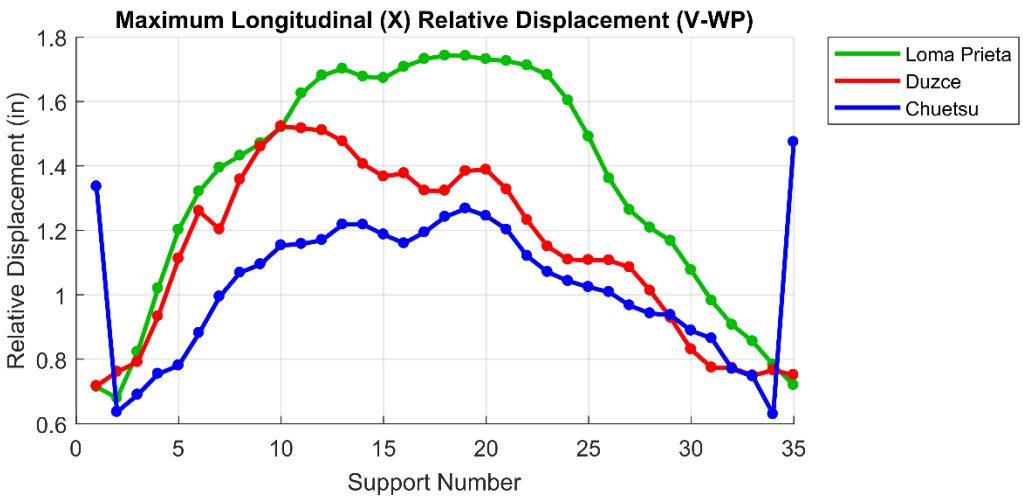


Figure 6.26. Maximum absolute longitudinal relative bent cap displacement

The maximum total bending moment was recorded for the columns at each support at plotted in Figure 6.27. Loma Prieta produced a maximum moment of 3.660E+7 lb-in at support 10. Duzce produced a maximum moment of 3.685E+7 lb-in at support 12. Chuetsu produced a maximum moment of 4.811E+7 lb-in at support 10. The shapes of the curves of maximum column moment closely resembled those of the maximum transverse relative displacement.

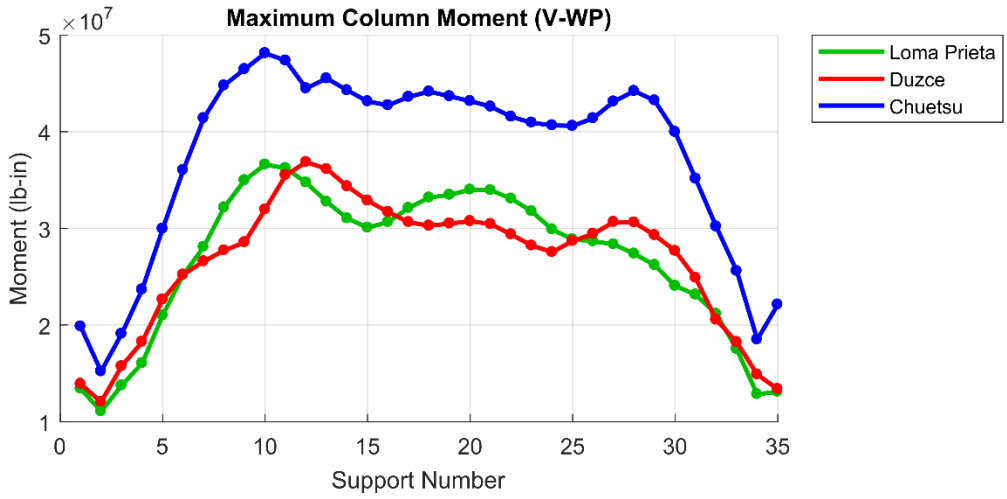


Figure 6.27. Maximum total column bending moment.

The time-history graphs of the relative transverse displacements of the bent caps are given in Figures 6.28, 6.29, and 6.30, which give the displacement response for Loma Prieta, Duzce, and Chuetsu, respectively. Each graph contains the time-history displacements of all supports plotted in the same window. The curves are color-coded according to *Graph Format A*. The response in all three cases appeared to be periodic, and the supports appeared to vibrate with proportional displacements. In contrast to the U-WP case, there appeared to be some minor permanent displacements that became more visible toward the end of the motion.

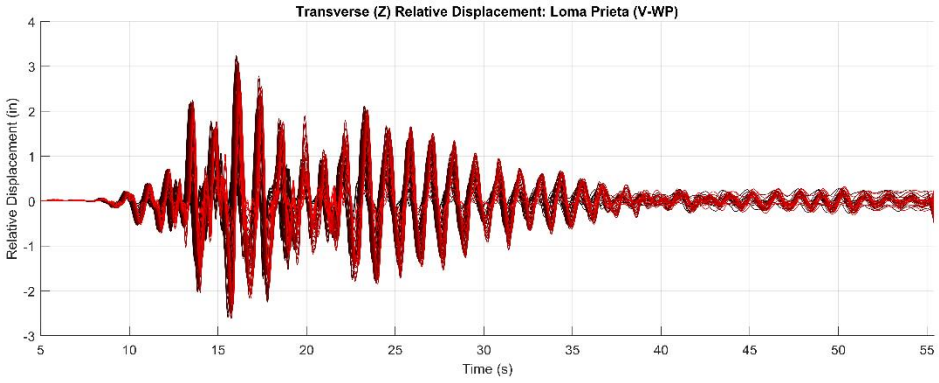


Figure 6.28. Relative transverse bent cap displacements for Loma Prieta.

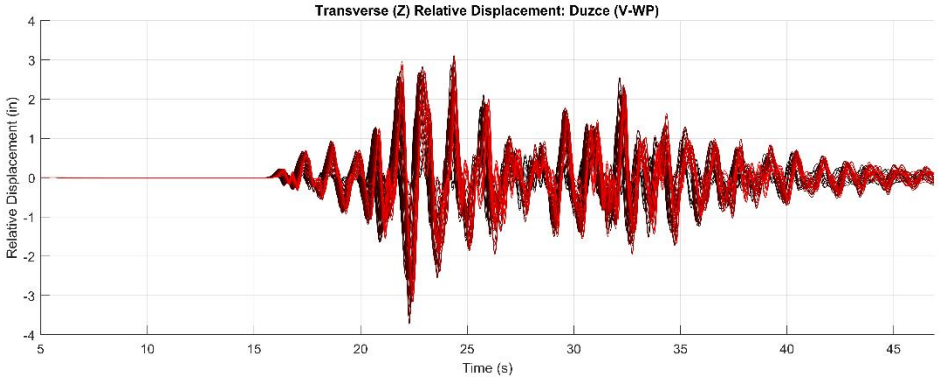


Figure 6.29. Relative transverse bent cap displacements for Duzce.

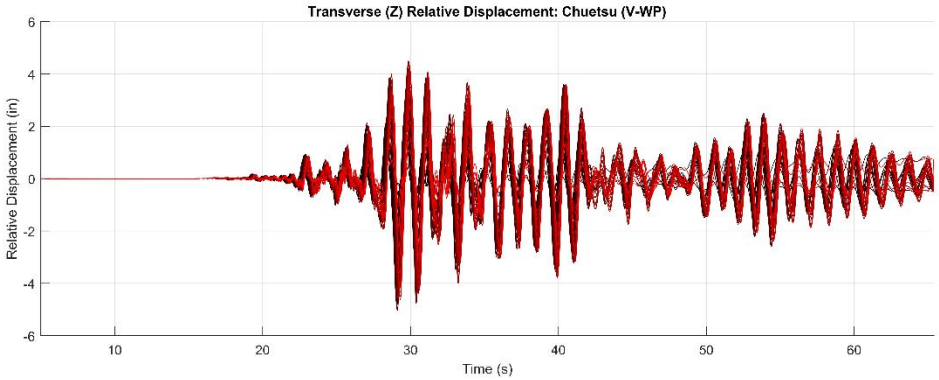


Figure 6.30. Relative transverse bent cap displacements for Chuetsu.

The time-history graphs of the relative longitudinal displacements of the bent caps are given in Figures 6.31, 6.32, and 6.33, which give the displacement response for Loma Prieta, Duzce, and Chuetsu, respectively. The graphs are color-coded using *Graph Format A*. As with the transverse displacement curves, the supports appeared to vibrate with proportional displacements and no noticeable phase shift. The longitudinal vibrations appeared to have higher frequencies than the corresponding transverse vibrations. The vibrations of the various supports appeared to be proportional to each other, and the motion appeared to be much less chaotic than in the corresponding graphs of the U-WP case.

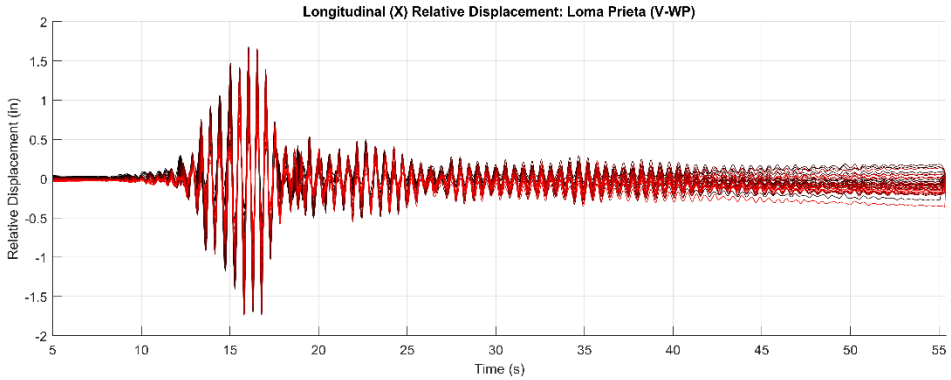


Figure 6.31. Relative longitudinal bent cap displacements for Loma Prieta.

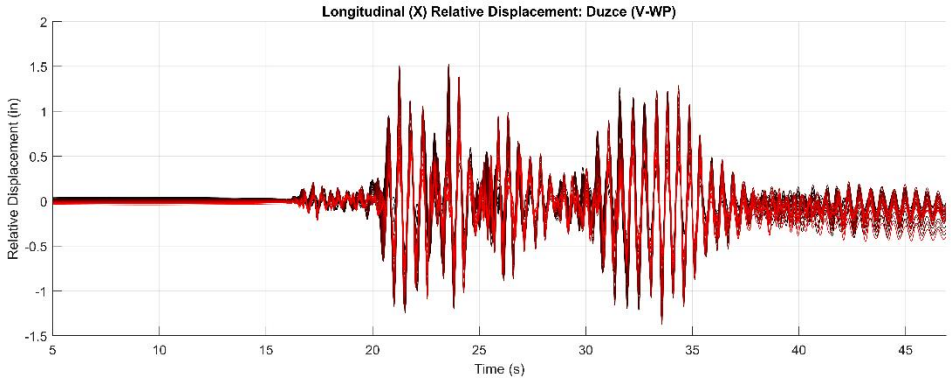


Figure 6.32. Relative longitudinal bent cap displacements for Duzce.

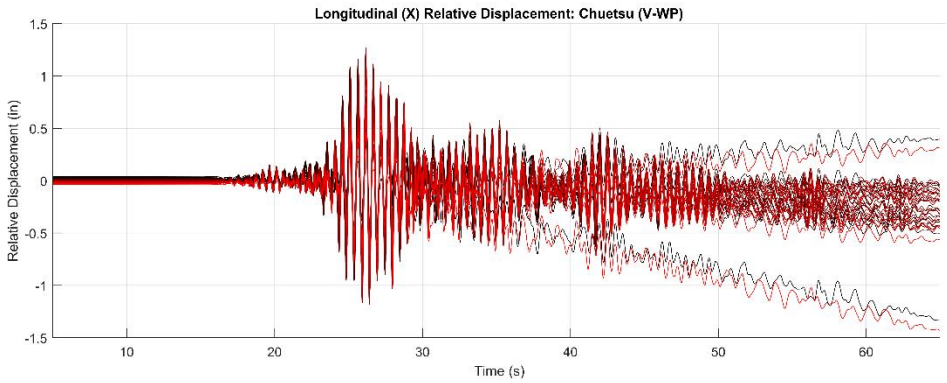


Figure 6.33. Relative longitudinal bent cap displacements for Chuetsu.

The kinetic, strain, and total energy curves are shown in Figures 6.34, 6.35, and 6.36 for Loma Prieta, Duzce, and Chuetsu, respectively. Loma Prieta produced a

maximum total energy of 3704.88 BTU at 15.4 sec. Duzce produced a maximum total energy of 2734.1 BTU at 21.99 sec. Chuetsu produced a maximum total energy of 3278.78 BTU at 29.44 sec.

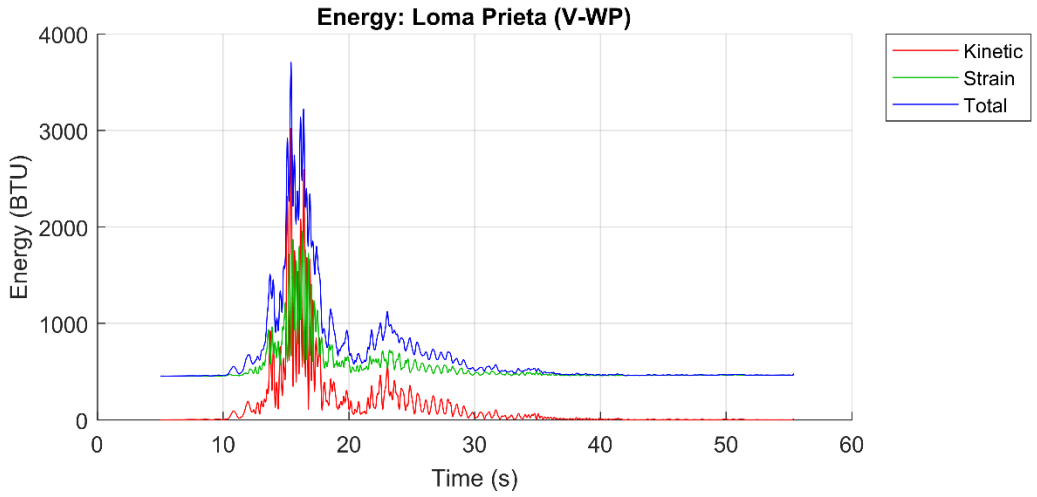


Figure 6.34. Kinetic, strain, and total energy for Loma Prieta.

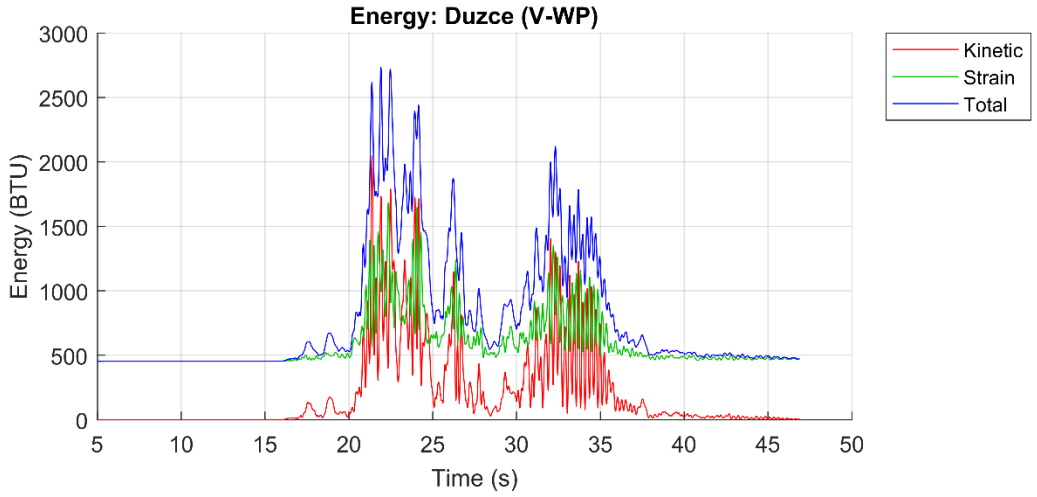


Figure 6.35. Kinetic, strain, and total energy for Duzce.

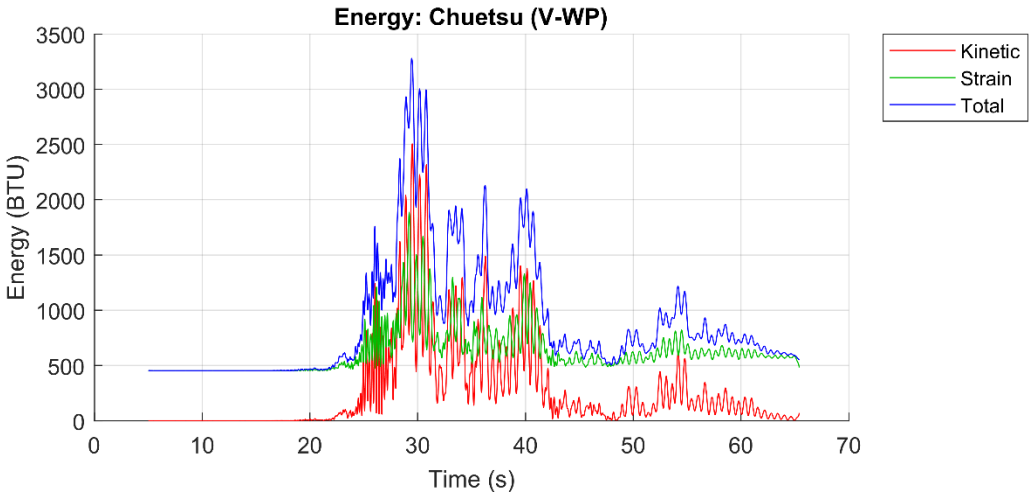


Figure 6.36. Kinetic, strain, and total energy for Chuetsu.

# CHAPTER 7: ANALYSIS AND DISCUSSION

## 7.1 Changes in Structural Response Due to Wave-Passage Effect

This section includes direct time-history comparisons between the responses of the experiments with consistent ground displacements (U-NW) and the experiments with wave passage effect and a uniform soil site (U-WP). An illustration technique is used in sections 6.1 and 6.2 which subtracts the former response quantity from the latter over the entire length of the earthquake. This produces a curve that represents the difference in an equivalent response quantity between first case (U-NW) and the second case (U-WP). In this difference curve, a positive value indicates that the latter quantity was greater than the former quantity, and a negative value indicates the reverse. In a periodic motion with a high frequency, this can be difficult to discern visually. To aid in the interpretation of the results, each time-history plot is paired with a trapezoidal rule time-integration of the curve. If the difference plot is balanced (equal parts positive and negative), then the integral should oscillate with a near-constant amplitude. If the difference plot is biased, the integral should indicate the direction of that bias. Both graphs use *Graph Format A*.

Using this technique, the relative transverse displacements of the bent caps were compared over time for all three earthquakes. The time-history difference graphs, which subtract the displacements in the U-NW case from those in the U-WP case, are given in Figures 7.1, 7.2, and 7.3 for Loma Prieta, Duzce and Chuetsu, respectively. The integral of the time-history difference graph for Loma Prieta shows that the response of the bridge was relatively well balanced when all supports are considered collectively. The graphs for the other two earthquakes exhibit similar behavior. This observation indicates that, by

including wave passage effect in the analysis, some supports experienced an increase in the amount of displacement-time, and some supports experienced a decrease.

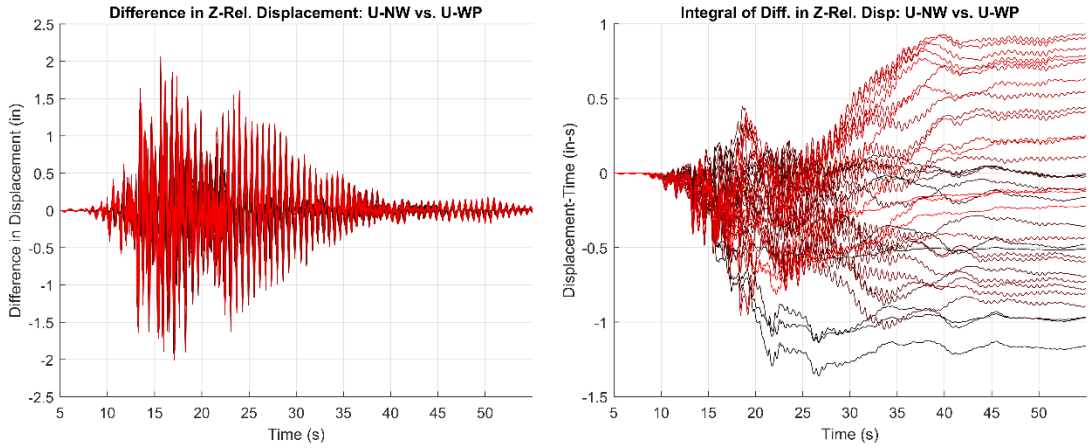


Figure 7.1. Time-history difference in relative transverse displacements (Loma Prieta).

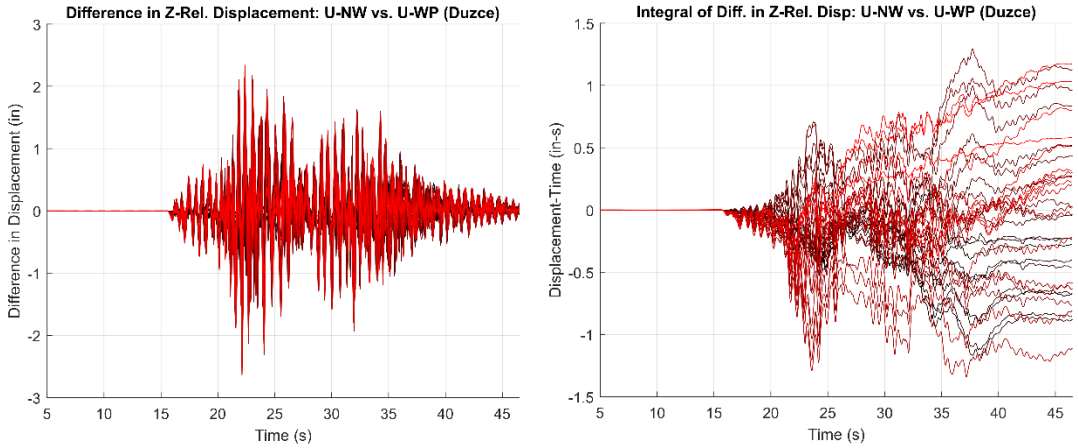


Figure 7.2. Time-history difference in relative transverse displacements (Duzce).

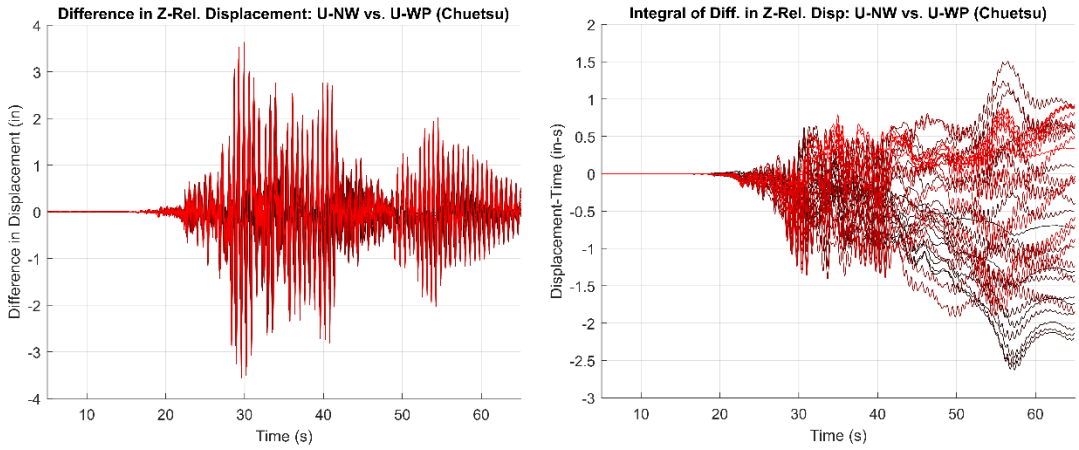


Figure 7.3. Time-history difference in relative transverse displacements (Chuetsu).

The relative longitudinal displacements of the bent caps were compared over time for all three earthquakes. The time-history difference graphs, which subtract the displacements in the U-NW case from those in the U-WP case, are given in Figures 7.4, 7.5, and 7.6 for Loma Prieta, Duzce and Chuetsu, respectively. In this case, all three earthquakes exhibited similar behavior, so they can be addressed collectively. The time-history difference plot and its integral exhibited a clear negative bias, indicating that the bent caps spent less time displaced and/or had lower maximum displacements in the U-WP case as compared with the U-NW case. Additionally, there is a very clear color gradient visible in the three integral graphs that indicates that the smallest decrease in relative displacement-time occurred near the ends of the bridge (red and black), and the largest decrease occurred near the midpoint of the bridge (burgundy).

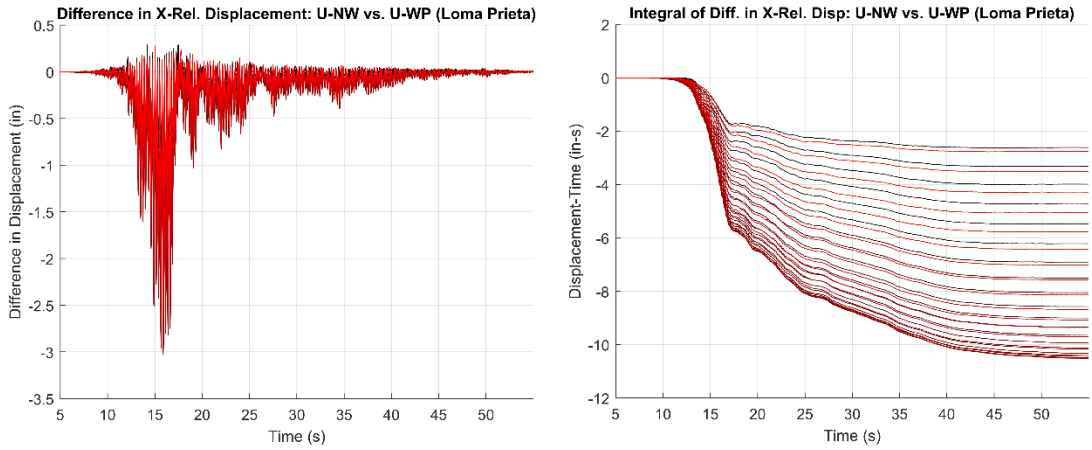


Figure 7.4. Time-history difference in relative longutudinal displacements (Loma Prieta).

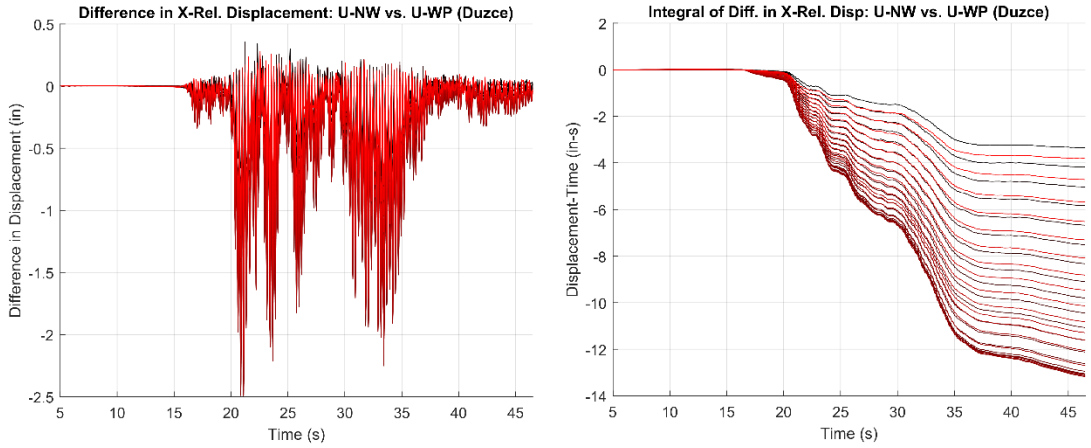


Figure 7.5. Time-history difference in relative longutudinal displacements (Duzce).

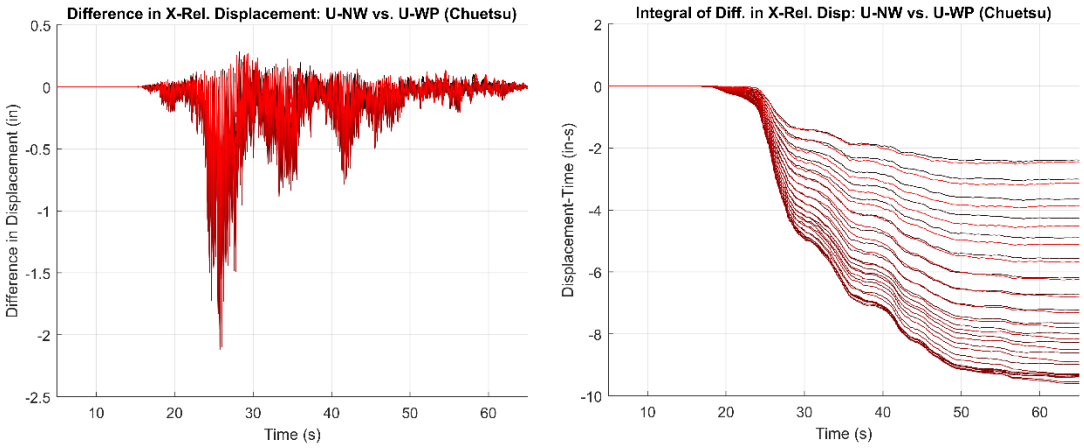


Figure 7.6. Time-history difference in relative longutudinal displacements (Chuetsu).

The maximum total bending moment values in the columns were compared over time for all three earthquakes. The time-history difference graphs, which subtract the moments in the U-NW case from those in the U-WP case, are given in Figures 7.7, 7.8, and 7.9 for Loma Prieta, Duzce and Chuetsu, respectively. Similar behavior was visible in the bending moment graphs to what was observed in the longitudinal relative displacement graphs. In all three earthquakes, the average bending moment over time decreased noticeably in the U-WP case as compared with the U-NW case.

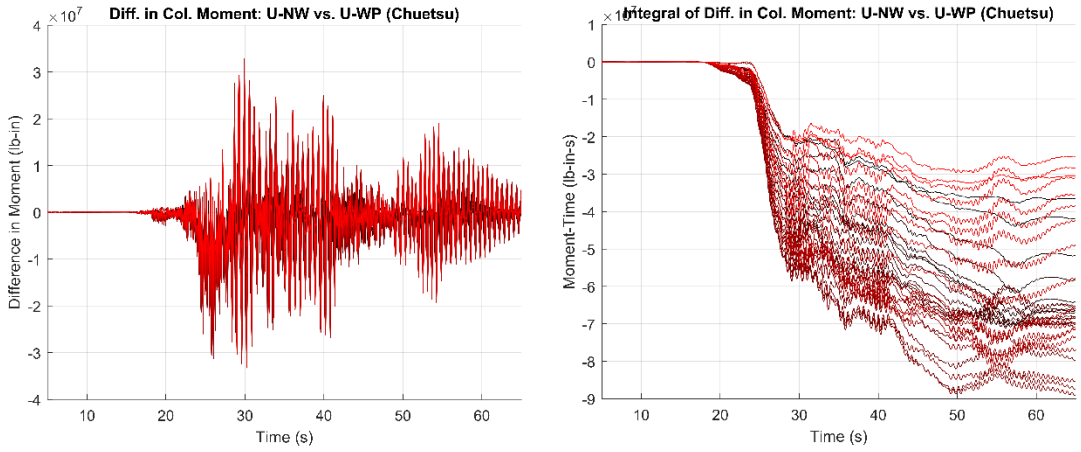


Figure 7.7. Time-history difference in column bending moment (Loma Prieta).

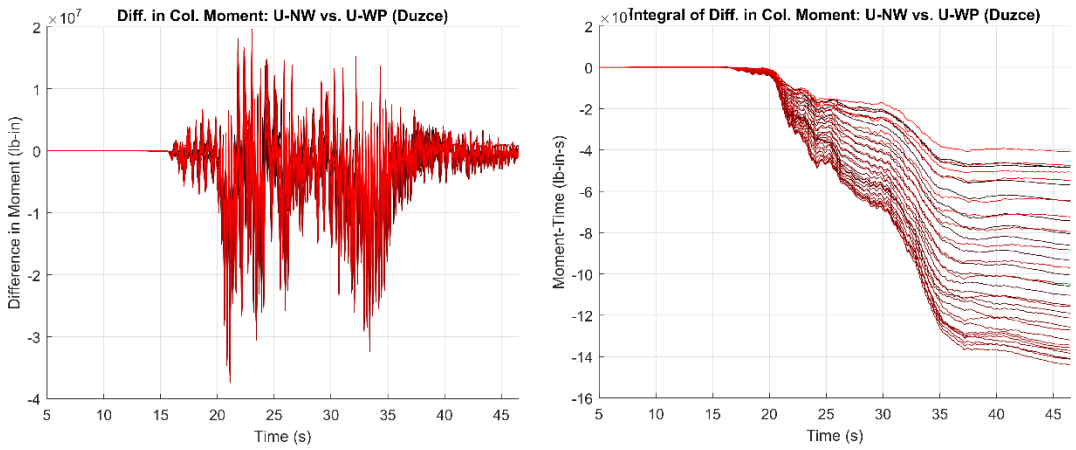


Figure 7.8. Time-history difference in column bending moment (Duzce).

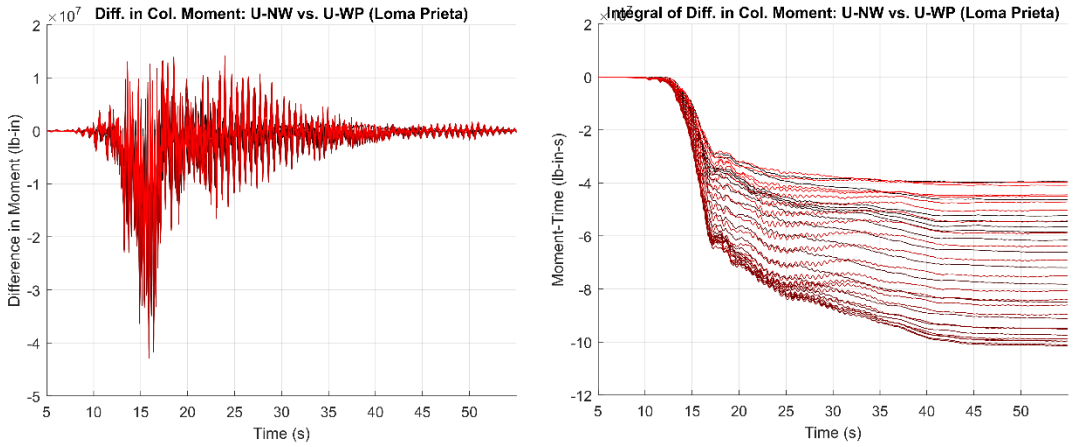


Figure 7.9. Time-history difference in column bending moment (Chuetsu).

## 7.2 Changes in Structural Response Due to Soil Profile Variability

This section includes direct time-history comparisons between the responses of the experiments with wave passage effect and a uniform soil site (U-WP) and the experiments with wave passage effect and a variable soil site (V-WP). Using the technique described in section 6.1, the relative transverse displacements of the bent caps were compared over time for all three earthquakes. The time-history difference graphs, which subtract the displacements in the U-WP case from those in the V-WP case, are

given in Figures 7.10, 7.11, and 7.12 for Loma Prieta, Duzce and Chuetsu, respectively. The time-history difference graphs had a similar behavior across all earthquakes. The integral plots show that the difference curves had a positive bias, indicating that the V-WP case had greater transverse relative displacements on average, as compared with the U-WP case. Additionally, the coloration of the graphs indicate that the difference was generally more pronounced near the midpoint of the bridge and less pronounced near the ends of the bridge.

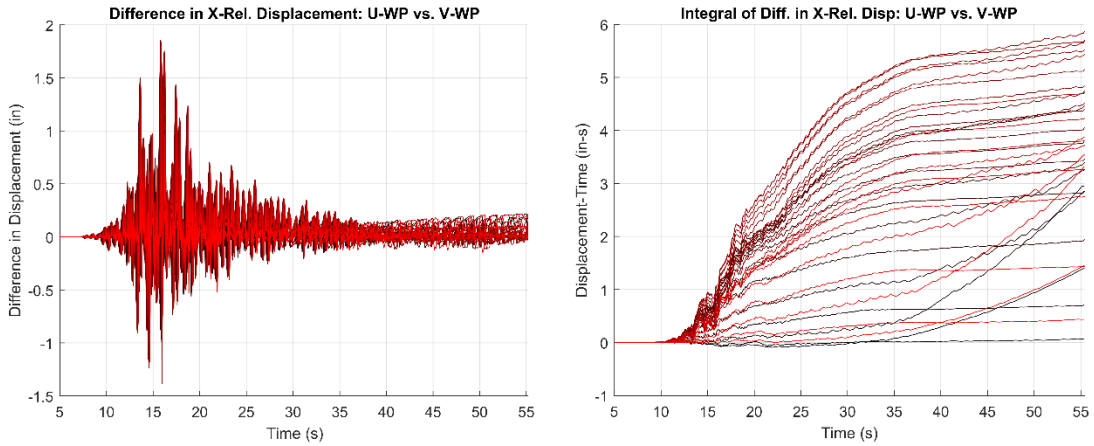


Figure 7.10. Time-history difference in relative transverse displacements (Loma Prieta).

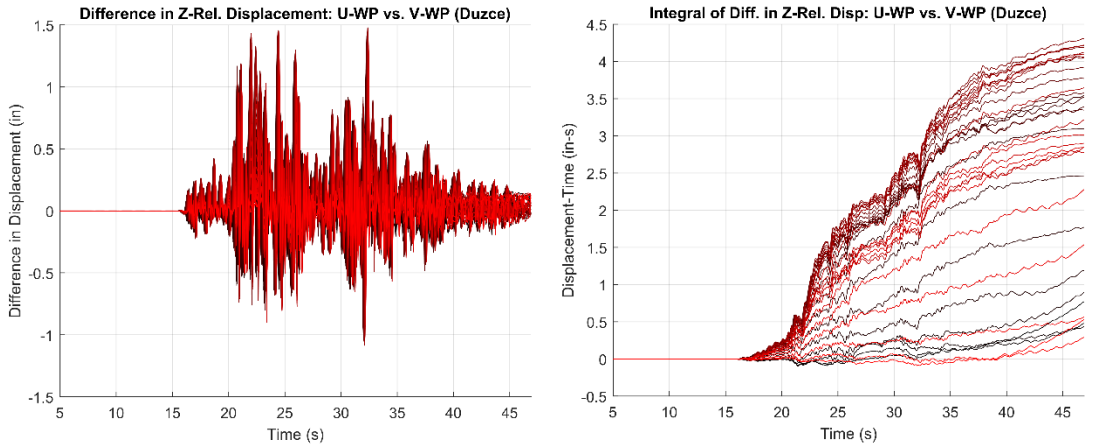


Figure 7.11. Time-history difference in relative transverse displacements (Duzce).

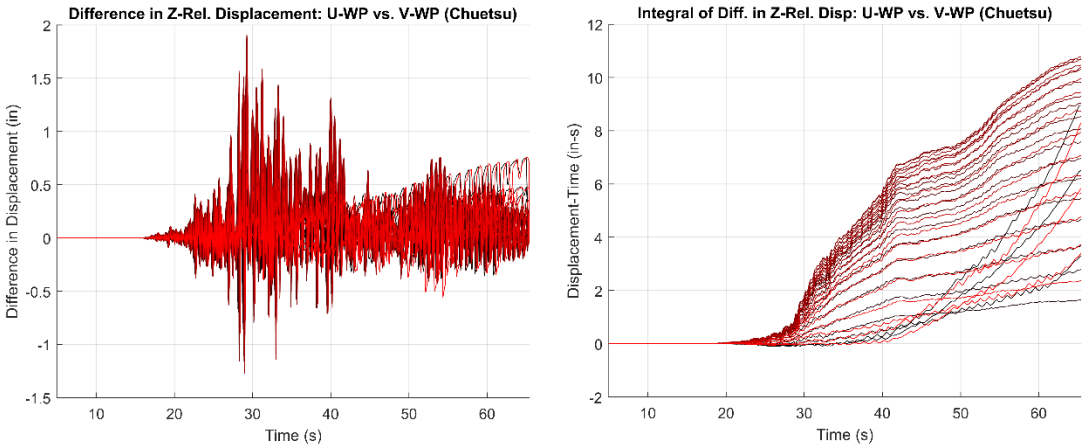


Figure 7.12. Time-history difference in relative transverse displacements (Chuetsu).

The relative longitudinal displacements of the bent caps were compared over time for all three earthquakes. The time-history difference graphs, which subtract the displacements in the U-WP case from those in the V-WP case, are given in Figures 7.13, 7.14, and 7.15 for Loma Prieta, Duzce and Chuetsu, respectively. The time-history difference graphs had a similar behavior across all earthquakes. The integral plots show that the difference curves had a positive bias, indicating that the V-WP case had greater longitudinal relative displacements on average, as compared with the U-WP case. Additionally, the coloration of the graphs indicate that the difference was generally more pronounced near the midpoint of the bridge and less pronounced near the ends of the bridge, with the exception of supports 1 and 35 in the Chuetsu earthquake, which experienced large permanent displacements toward the end of the motion.

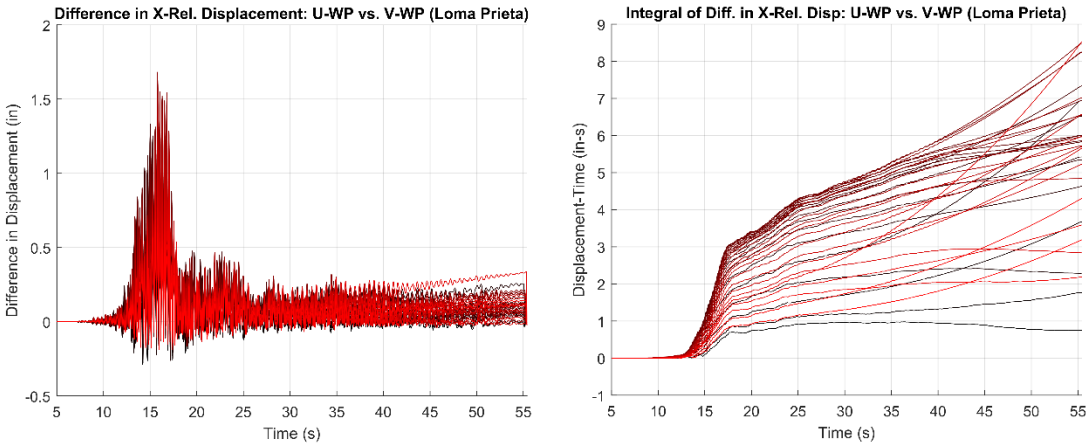


Figure 7.13. Time-history difference in relative longutudinal displacements (Loma Prieta).

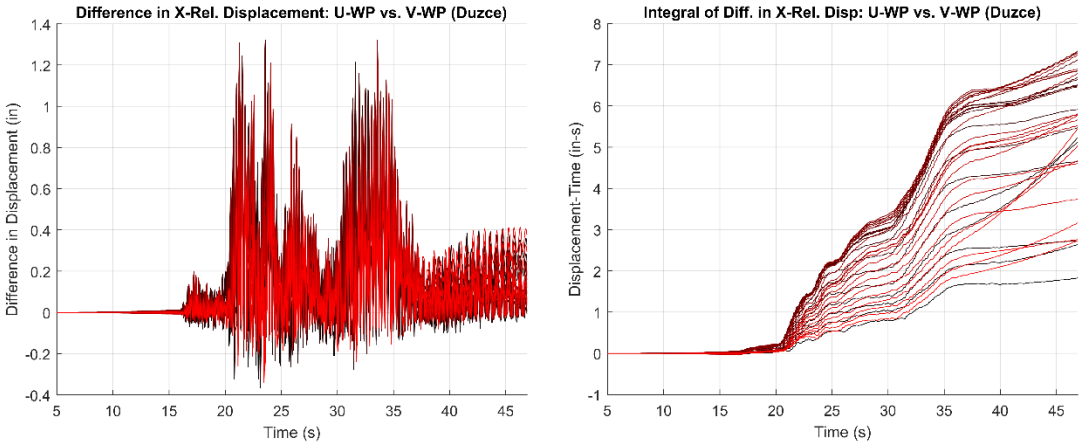


Figure 7.14. Time-history difference in relative longutudinal displacements (Duzce).

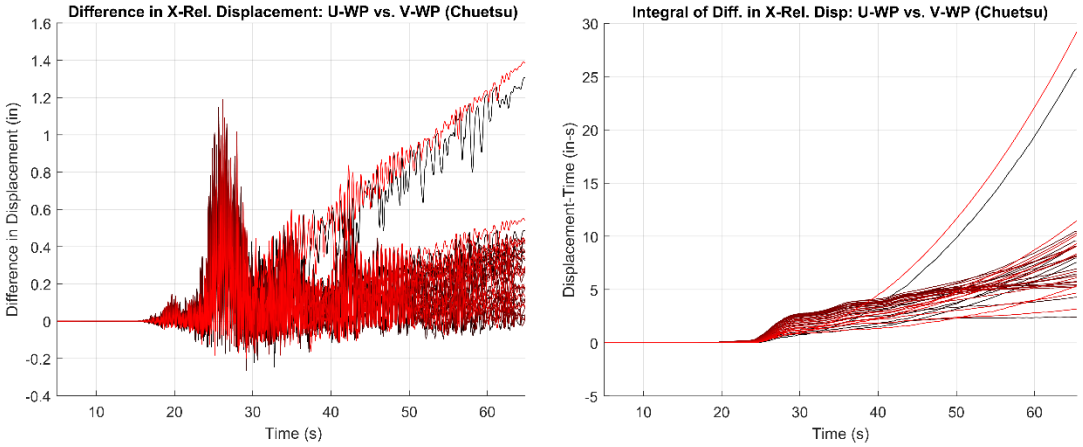


Figure 7.15. Time-history difference in relative longutudinal displacements (Chuetsu).

The maximum total bending moment values in the columns were compared over time for all three earthquakes. The time-history difference graphs, which subtract the moments in the U-WP case from those in the V-WP case, are given in Figures 7.16, 7.17, and 7.18 for Loma Prieta, Duzce and Chuetsu, respectively. The time-history difference plots of column bending moment had similar characteristics to those of longitudinal relative displacement. It should be noted that the percentage change in the maximum relative longitudinal displacement between the U-WP case and the V-WP case was significantly larger than the corresponding change in the relative transverse displacement (see section 6.3). This was likely the reason that the changes in column bending moment appeared to parallel the changes in relative longitudinal displacement.

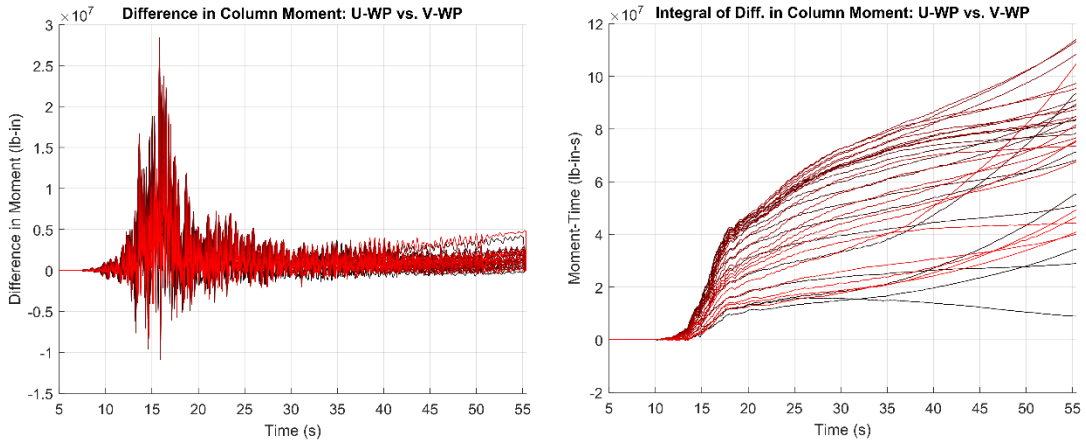


Figure 7.16. Time-history difference in column bending moment (Loma Prieta).

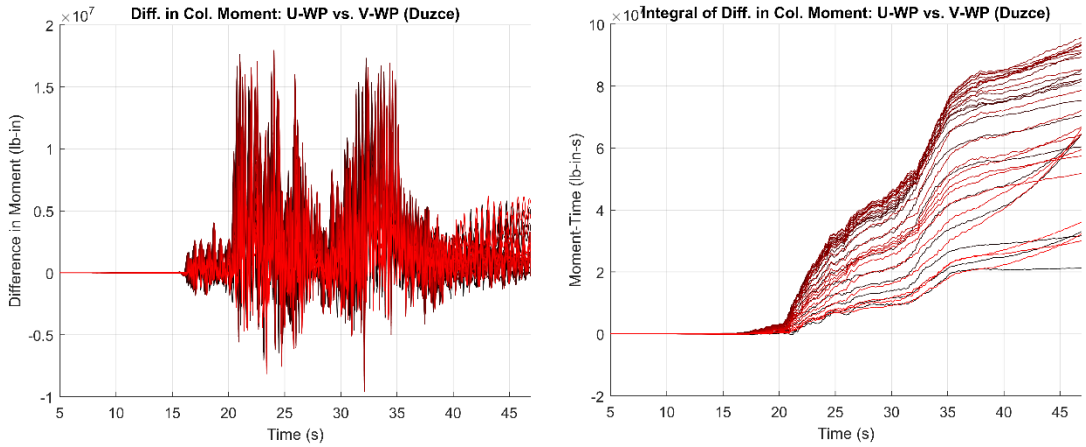


Figure 7.17. Time-history difference in column bending moment (Duzce).

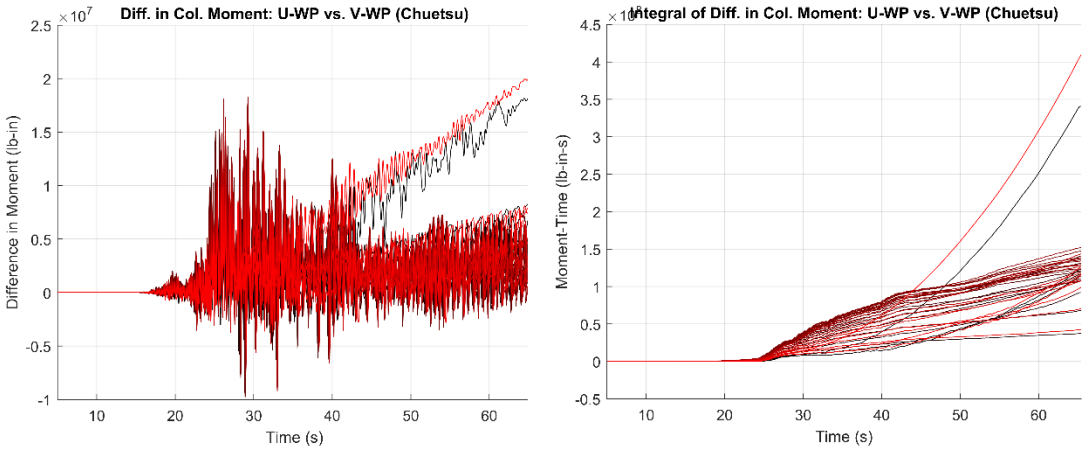


Figure 7.18. Time-history difference in column bending moment (Chuetsu).

## 7.3 Other Metrics

The total energy of the model is plotted with respect to time in Figures 7.19, 7.20, and 7.21 for Loma Prieta, Duzce and Chuetsu, respectively. The Loma Prieta plot showed a significant difference in peak total energy between the test cases, with the U-NW case having a peak total energy that was 5.75 times that of the U-WP case and 2.17 times that of the V-WP case. A similar proportionality appeared to remain throughout the energy spike that occurred at around 16 sec. The Duzce energy plot showed the maximum total energies of the test cases to fall in the same order, with the U-NW case having a peak total energy that was 3.35 times that of the U-WP case and 2.08 times that of the V-WP case. The peaks in energy occurred at approximately the same time values, though there existed an initial energy spike (containing the maximum) in the U-NW case that did not have clear counterparts in the other two cases. In the Chuetsu plot, the U-NW case had a peak total energy that was 1.45 times that of the U-WP case and 1.04 times that of the V-WP case. Thus, there was significantly less variation in the total energy for Chuetsu than

for the other two earthquakes. The peak energy value of the U-NW case preceded that of the U-WP case by 3.83 sec and that of the V-WP case by 3.80 sec.

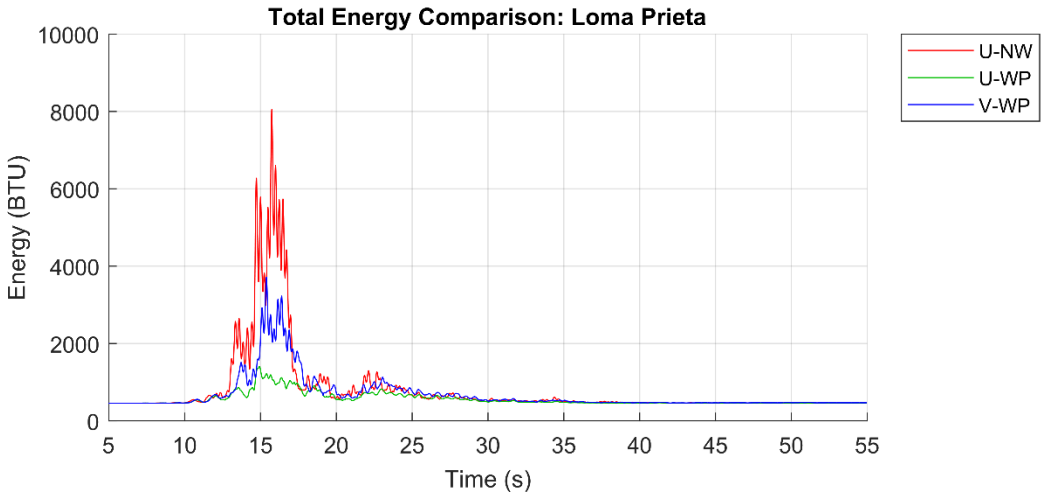


Figure 7.19. Total system energy for Loma Prieta.

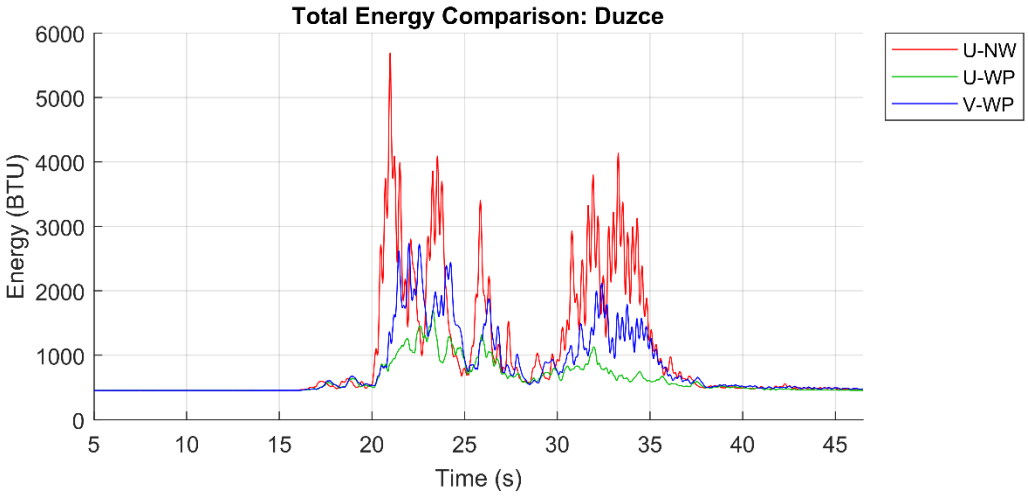


Figure 7.20. Total system energy for Duzce.

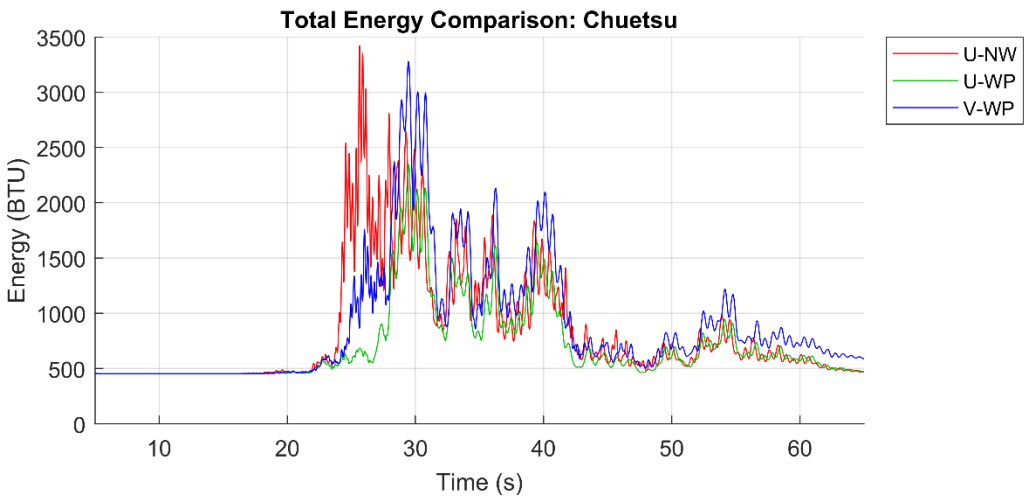


Figure 7.21. Total system energy for Chuetsu.

The maximum relative transverse bent-cap displacements are plotted in Figures 7.22, 7.23, and 7.24 for Loma Prieta, Duzce and Chuetsu, respectively. The observations were similar for all three earthquakes, with the V-WP case resulting in the largest maximum displacement at most supports, and the U-NW and U-WP cases having similar maximum displacements throughout the length of the bridge.

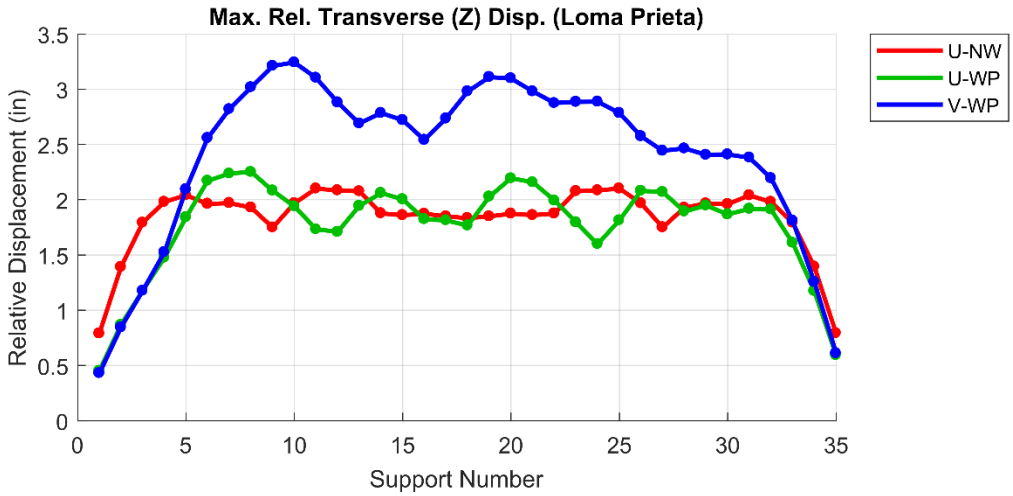


Figure 7.22. Maximum relative transverse bent cap displacements for Loma Prieta.

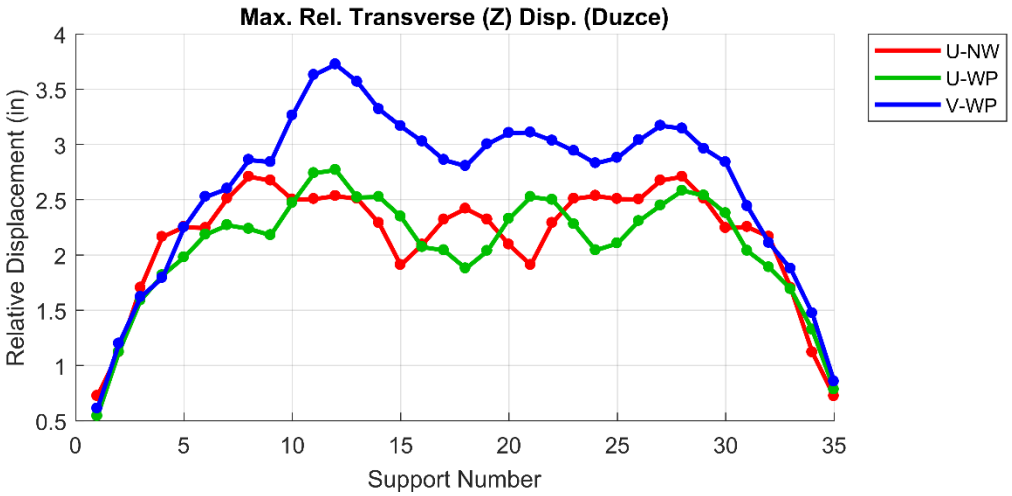


Figure 7.23. Maximum relative transverse bent-cap displacements for Duzce.

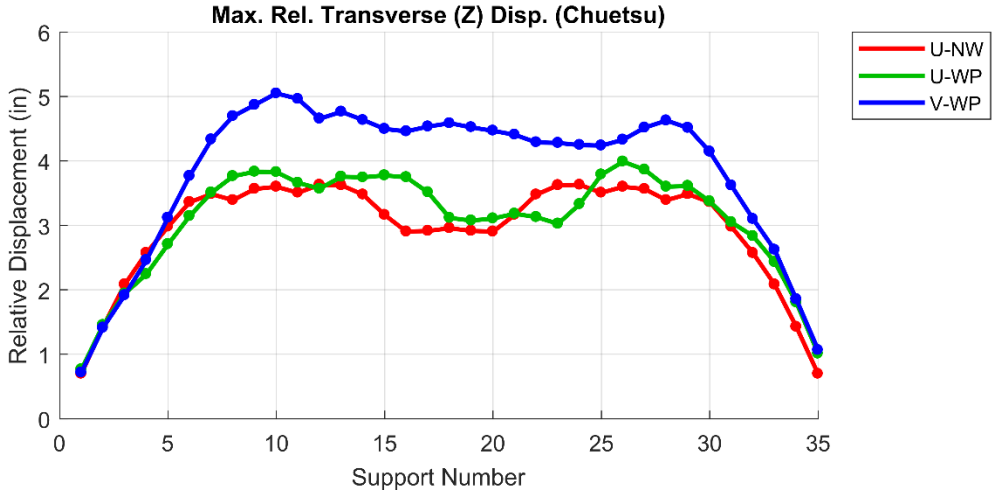


Figure 7.24. Maximum relative transverse bent-cap displacements for Chuetsu.

The maximum relative longitudinal bent-cap displacements are plotted in Figures 7.25, 7.26, and 7.27 for Loma Prieta, Duzce and Chuetsu, respectively. For all earthquakes, the U-NW case had the largest displacement at each support and the V-WP case had the second largest displacement at each support, with the exception of supports 1 and 35 in the Chuetsu earthquake, at which the V-WP case had the largest

displacements. In all earthquakes and all supports, the U-WP case had the smallest displacements.

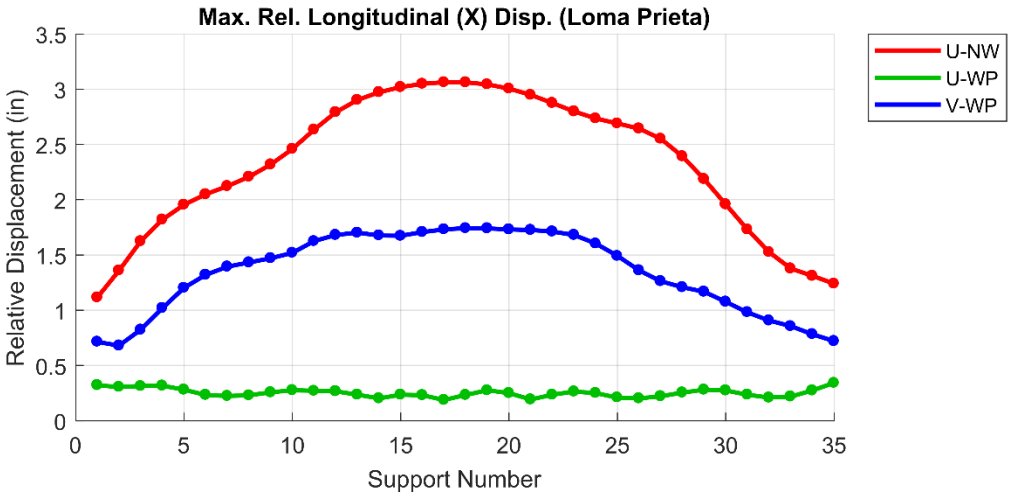


Figure 7.25. Maximum relative longitudinal bent-cap displacements for Loma Prieta.

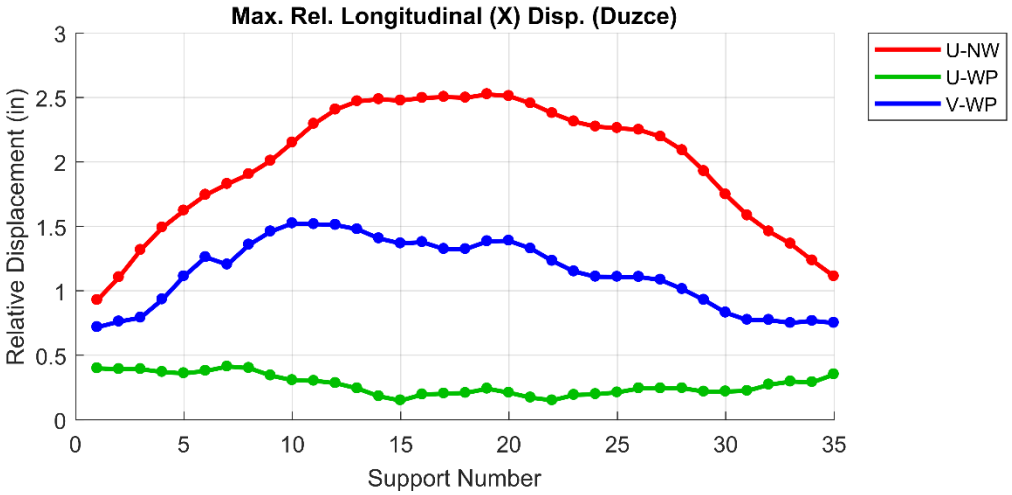


Figure 7.26. Maximum relative longitudinal bent-cap displacements for Duzce.

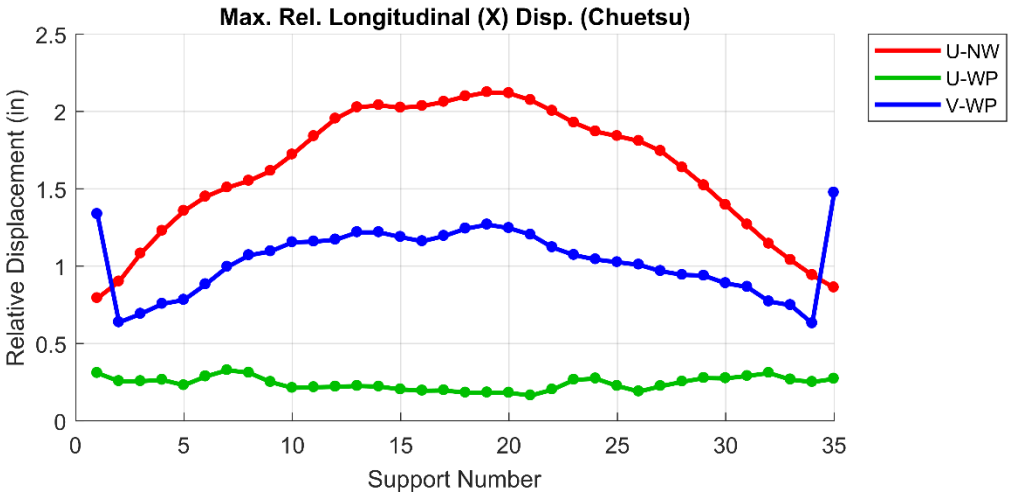


Figure 7.27. Maximum relative longitudinal bent-cap displacements for Chuetsu.

The maximum column moments are plotted in Figures 7.28, 7.29, and 7.30 for Loma Prieta, Duzce and Chuetsu, respectively. In the Loma Prieta and Duzce earthquakes, the maximum moments, in general, were greatest in the U-NW case, followed by V-WP, followed by U-WP. In the Chuestu earthquake, the maximum moments were approximately equal between the U-NW case and the U-WP case. The V-WP case had the largest maximum bending moments.

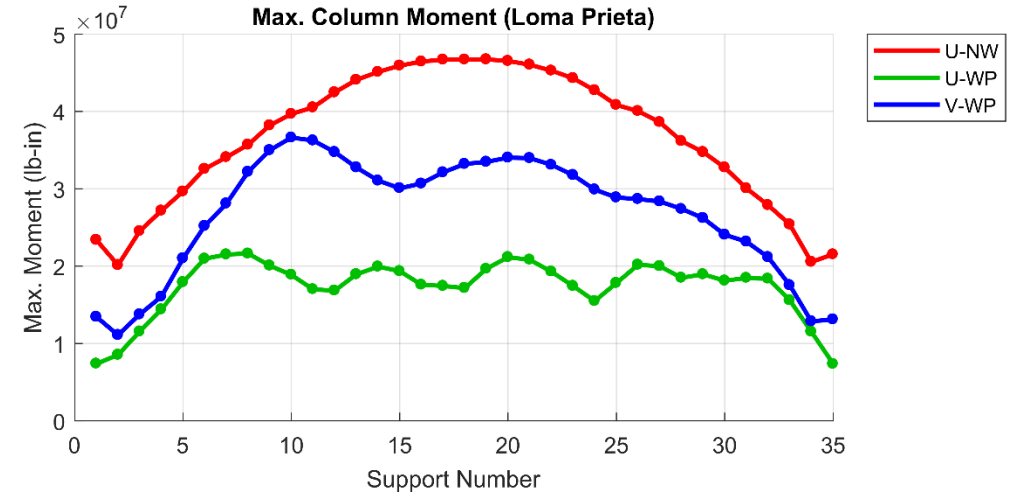


Figure 7.28. Maximum column moments for Loma Prieta.

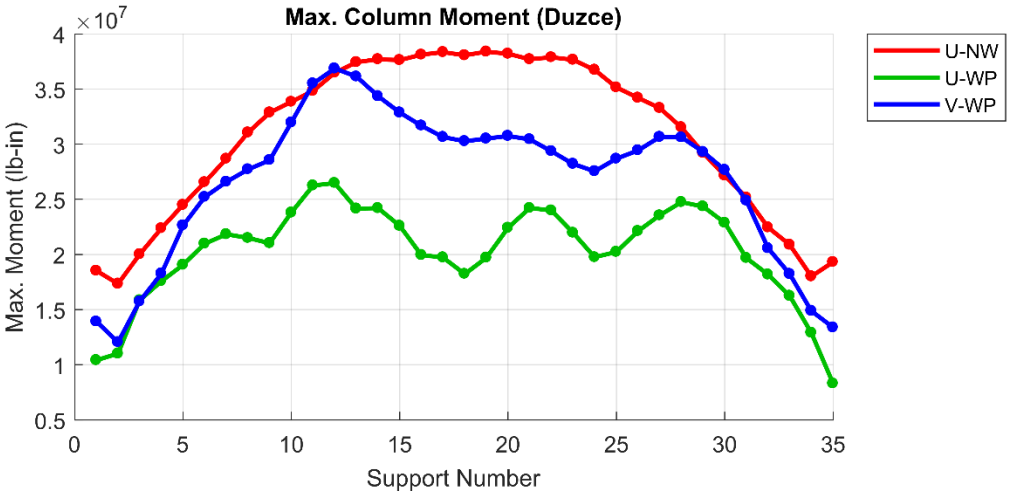


Figure 7.29. Maximum column moments for Duzce.

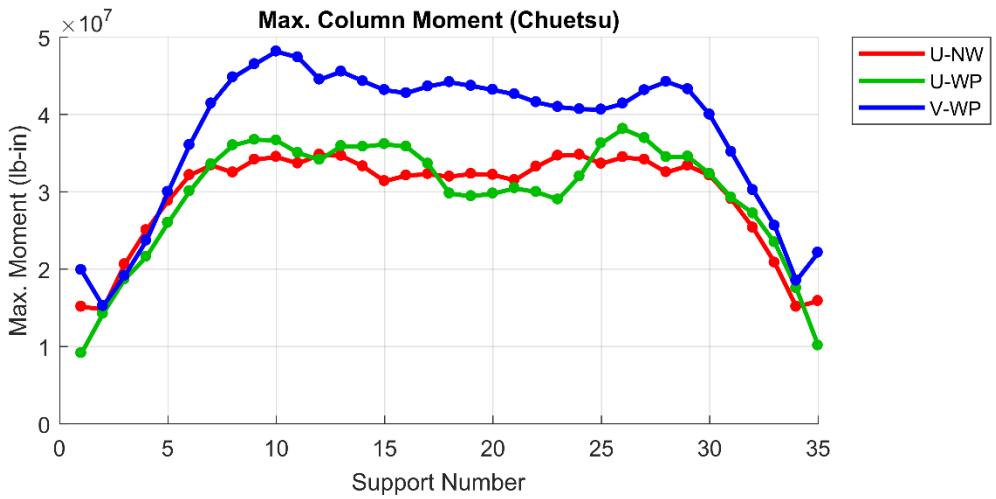


Figure 7.30. Maximum column moments for Chuetsu.

# CHAPTER 8: CONCLUSIONS

This report summarized the development and testing of a long bridge model subject to consistent ground displacements (U-NW), ground displacements with wave passage effect and no soil variability (U-WP), and ground displacements with both wave passage effect and soil variability (V-WP). The model utilized coupled foundation stiffness matrices as a soil-structure interaction model, and linearized stiffness convergence was achieved. A site response analysis was conducted on six earthquake time-history records, and permanent surficial displacements were obtained. The following conclusions were made.

1. Adding only wave passage effect to the U-NW case decreased the relative longitudinal displacements of the bridge deck.
2. Adding only wave passage effect to the U-NW case decreased the maximum total energy of the bridge model.
3. The V-WP case resulted in greater maximum transverse relative displacements at nearly all bridge supports than the U-NW case and the U-WP case.
4. In general, the case with no wave passage or soil variability (U-NW) had the greatest total energy throughout most of the earthquake duration.
5. Maximum longitudinal relative displacement correlates with the maximum total system energy.

# REFERENCES


Ashnaashari, M., Grafton, R., and Johnnie, M. (2005). Precast Concrete Design-Construction of San Mateo-Hayward Bridge Widening Project. PCI Journal 50(1) (January 2005), pp. 26-43.

Elder, W. (2013). Bedrock geology of the San Francisco Bay Area: A local sediment source for bay and coastal systems. Marine Geology, 345, pp. 18-30.

Hayward Fault Scenarios. (n.d.). Retrieved from https://earthquake.usgs.gov/learn/topics/shakingsimulations/hayward/

Hudnut, K., Wein, A. Cox, D., Porter, K., Johnson, L., Perry, S., Bruce, J. and LaPointe, D. (2018). The Haywired Earthquake Scenario-We Can Outsmart Disaster. USGS Fact Sheet 2018-3016, U.S. Geological Society, U.S. Department of the Interior.

Kavazanjian, E, Wang, J-N, Martin, G., Shamsabadi, A., Po Lam, I., Dickenson, S., and Hung, C. (2011). LRFD Seismic Analysis and Design of Transportation Geotechnical Features and Structural Foundations Reference Manual. NHI Course No. 130094, Report No. FHWA-NHI-11-032. FHWA: Washington, DC.

Lam, I. and Law, H. (2000). Soil structure interaction of bridge for seismic analysis. Technical Report MCEER 00-0008, University at Buffalo, The State University of New York.

Marsh, M., Buckle, I, Kavazanjian, E. (2014). LRFD Seismic Analysis and Design of Bridges Reference Manual. NHI Course No. 130093 and 130093A, Report No. FHWA-NHI-15-004. FHWA: Washington, DC.

Mayne, P. (2007). Cone penetration testing state-of-practice. Final Report NCHRP Project 20-05, Topic 37-14. Transportation Research Board, Washington, D.C.

PEER Ground Motion Database. (n.d.). https://ngawest2.berkeley.edu/

USACE (U.S. Army Corps of Engineers). (2015). South San Francisco Bay Shoreline Study (SSFBS). Appendix G: Geotechnical Engineering, September, 2015.

Wilcox, G. and Van Velsor, J. (1995). Geotechnical report for environmental study, Route 92 widening at the San Mateo-Hayward Bridge. Report 04174-003050, Office of Structural Foundations, Engineering Service Center, Department of Transportation, State of California.